FOR BRIGHTER ELECTRON SOURCES: A CRYOGENICALLY COOLED PHOTOCATHODE AND DC PHOTOGUN

A Dissertation

Presented to the Faculty of the Graduate School

of Cornell University

in Partial Fulfillment of the Requirements for the Degree of

Doctor of Philosophy

by

Hyeri Lee

August 2017

FOR BRIGHTER ELECTRON SOURCES:

A CRYOGENICALLY COOLED PHOTOCATHODE AND DC PHOTOGUN

Hyeri Lee, Ph.D.

Cornell University 2017

Electron beams produced by photoinjectors have a wide range of applications including colliders for high energy and nuclear physics experiments, Free Electron Lasers (FEL), Energy Recovery Linacs (ERL), and Ultrafast Electron Diffraction (UED) with a variety of uses. These applications have been made possible by recent advancement in photocathode and photoinjector research. The key factor is building a compact high-brightness electron source with high voltage and electric field at the photocathode to maximize the electron emission and minimize emittance growth due to space-charge effect. Achieving high brightness from a compact source is a challenging task because it involves an often-conflicting interplay between various requirements imposed by photoemission, acceleration, and beam dynamics. This thesis presents three important results; (i) cryogenically cooled photocathode. From 300K to 90 K, the MTE reduction has been measured from 38 $\pm$ 2 meV to 22 $\pm$ 1 meV. (ii) transmission photocathode. MTEs generated from the photocathode operated in transmission mode is smaller by 20% in comparison with the reflection mode operation, which is accompanied by a corresponding QE decrease of about a factor of 2. (iii) a new design of a DC photoemission gun and beamline constructed at Cornell University, along with demonstration of a cryogenically cooled photocathode and transmission photocathode. This photoemission gun can operate at $\sim$200 kV at both room temperature (RT) and cryogenic temperature (low T) with a corresponding electric field of 10 MV/m.

Biographical Sketch

Hyeri Lee was born in Seoul, South Korea on September 1st 1986. She was a shy but independent and brave girl who took her time to decide what she wants at her own pace. She was fascinated by stars in the night sky and became interested in physics. She obtained her Bachelors with a major in Physics from Sogang University, Seoul, South Korea in 2011. She also spent the 2010 spring semester at Illinois Institute of Technology in Chicago as an exchange student.

In the fall of 2011, Hyeri joined the physics Ph.D. program at Cornell University. She chose accelerator physics due to its broad impacts on science and technology. Her work mainly focused on developing and characterizing ultra-cold electron photocathodes used as electron sources for various accelerator and ultra-fast imaging applications. After graduation she will begin working at Harvard Medical School in a medical physics residency program.

During her time at Cornell, Hyeri learned what physics entails and how to enjoy life while going through difficulties.

To my parents and family:

for their unlimited love and endless support.

Acknowledgments

This work could not have been done without the help of many whom I deeply thank. First of all I would like to express immense thanks to my advisor Prof. Ivan Bazarov for his guidance and support in my research. I am also thankful to Dr. Luca Cultrera from who I learned what an experimental physicist should do and Tobey Moore, the best technician and handyman in the world. Their help and expertise were invaluable to my work.

I would like to give a special note of thanks to Dr. Bruce Dunham, Dr. Xianghong Liu, Dr. Adam Bartnik, Karl Smolenski, John Dobbins, Prof. Val Kostroun, Peter Quigley, Prof. James Sethna, Prof. Lena Kourkoutis and senior graduate students - Colwyn Gulliford, Jared Maxson, Siddharth Karkare, Steve Full and Heng Li and also members of Wilson and Newman Laboratory for their input and assistance through my Ph.D.

I would also like to thank all the undergraduate, REU and master students who were able to produce useful work under my guidance and help in various aspects of my Ph.D work. I acknowledge my friends for their company and friendship: Ajay, Kaumudi, Deniz and 4C members.

My husband Stephen and my first roommate Annie Nit have stood by me, helping with every step from day one at Cornell. I cannot imagine my life without these two. I owe special thanks to all my family back in Korea and in Ohio for their unconditional love and endless support.

Research in this thesis was supported by the National Science Foundation (Grant No. PHY-1416318) and the Department of Energy (Grants No. DE-SC0014338 and No. DE-SC0011643).

Table of Contents

List of Figures

List of Tables

CHAPTER 1

Introduction

1.1 Ultra Bright Electron Beams

1.1.1 Background and Definition

Ultra bright electrons enhance the performance of accelerators and make new applications of accelerators possible[8–11]. Photoinjectors produce ultra bright electrons from a photoemissive material — the photocathode. An electron beam is formed as electrons are excited via a laser with photon energy $h\nu$, emitted to the vacuum and then accelerated in an electric field. Electron beams produced by photoinjectors have a wide range of applications including colliders for high energy and nuclear physics experiments, Free Electron Lasers (FELs), and Energy Recovery Linacs (ERL) with a variety of uses. The development of photocathodes and photoinjectors has become a critical technology and science research making these applications possible.

Another important application is electron imaging. In this field, electron beams are used to image the sample via electron diffraction or electron microscopy. Electron imaging used to study dynamic systems with ultrashort bunch length is called ultrafast electron imaging. Ultrafast Electron Diffraction (UED)[12], one of the ultrafast electron imaging techniques, uses bright electrons to observe atomic level dynamics. In order to obtain a clear diffraction

pattern within a single shot, UED needs a short enough bunch length with sufficiently long coherence length at the sample location.[11, 13–17] Among dynamic systems with various spatiotemporal scales, scientists are eager to study biomolecules, e.g. proteins, via a single-shot UED to observe highly complicated atomic motion exerting the biological functions. The upper limit to the crystal unit cell size resolvable by this approach is set by how bright the electron beams produced by a photoinjector are.

In order to understand the brightness, it is necessary first to define a key figure merit for photoemission, the so-called intrinsic emittance. Photoemission of electrons is commonly explained using the Spicer's three-step model[18] shown in Fig. 1.1: (i) photoexcitation of electrons (ii) transport of the excited electrons to the vacuum surface and (iii) the escape of the electrons through the vacuum barrier. Assuming that electrons are emitted isotropically with no correlation between transverse position and momentum ($\langle xp_x \rangle = 0$), the intrinsic emittance $\epsilon_{i,x}$ can be expressed as a function of the mean transverse energy (MTE) of the emitted electrons at the photocathode surface as following:

$$\epsilon_{i,x} = \frac{\sqrt{\langle x^2 \rangle \langle p_x^2 \rangle - \langle xp_x \rangle^2}}{m_e c} = \sigma_{i,x} \frac{\sqrt{\langle p_x^2 \rangle}}{m_e c} = \sigma_{i,x} \sqrt{\frac{\mathrm{MTE}}{m_e c^2}} = \sigma_{i,x} \sqrt{\frac{kT_e}{m_e c^2}} \tag{1.1}$$

where kT_e is the effective temperature of the emitted electrons, $\sigma_{i,x}$ is the rms laser spot size, $\langle p_x^2 \rangle$ is the transverse momentum variance, $m_e c^2$ is the electron rest mass in eV.

Recent studies extend Spicer's model to include the effects of a finite temperature of the electron gas to better explain their experimental results[7, 19, 20]. According to these studies, the photoemission occurring when excited with photon energy close to the photocathode workfunction has the MTE of photoelectrons limited by the lattice temperature for both metals and semiconductors. Electron photoemission has been also observed for the photons with energy lower than the metals workfunction or the sum of the energy gap and the electron affinity for semiconductors because of non-zero probability of

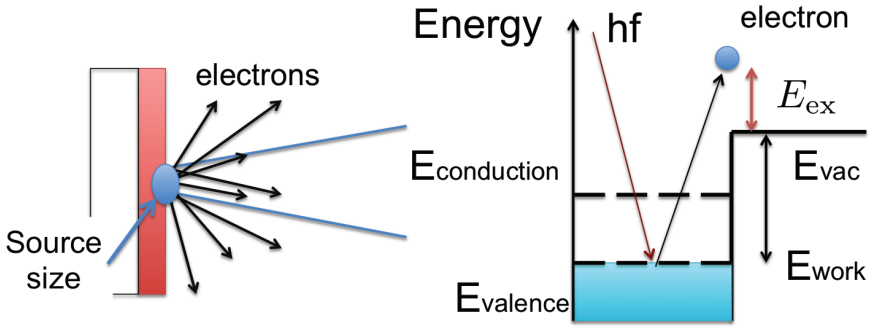

Figure 1.1: Photoemission process: $E_{conduction}$: Conduction band minimum, $E_{valence}$: Valence band maximum, E_{work}: work function, hf: photon energy, E_{vac}: vacuum barrier, E_{ex}: excess energy (hf-E_{work})

having electrons above the Fermi energy due to the finite temperature or the impurity and defect states of the semiconductors localized in the energy gap. Within the model accounting for the finite temperature, the MTE can be written as[7]:

$$\text{MTE} = kT\frac{Li_3[-\exp[\frac{1}{kT}(h\nu - E_{work})]]}{Li_2[-\exp[\frac{1}{kT}(h\nu - E_{work})]]} \tag{1.2}$$

where Li_n is the polylogarithm function defined as

$$Li_n[z] = \frac{(-1)^{n-1}}{(n-2)!}\int_0^1 \frac{1}{t}Log[t]^{n-2}Log[1-zt]dt. \tag{1.3}$$

At the charge saturation limits[21, 22], the intrinsic emittance $\epsilon_{i,x}$ is set by E_{cath} and the charge q;

$$\epsilon_{i,x} \propto \sqrt{\frac{\text{MTE}}{m_e c^2}} \begin{cases} (\frac{q}{E_{\text{cath}}})^{1/2}, & \text{“pancake”}, A \gg 1 \\ \frac{1}{E_{\text{cath}}}(\frac{q}{\sigma_{i,t}})^{2/3}, & \text{“cigar”}, A \leq 1 \end{cases} \tag{1.4}$$

depending on the laser pulse length $\sigma_{i,t}$, bunch charge q, electric field at cathode E_{cath} and the initial beam aspect ratio A ($= \sigma_{i,x}/(\frac{eE_{\text{cath}}}{m_e c^2})(c\sigma_{i,t})^2$)[23, 29].

The beam brightness is defined as the phase space density, the number of particles per unit volume in the 6D phase space where the emittance is the phase space area for the

respective 2D subspace. For a relativistic beam, the motion along the beam propagation direction is largely independent of the motion in the transverse planes. The transverse normalized phase space, (x, y, $\gamma\beta_x$, $\gamma\beta_y$), and the corresponding brightness, $B_{n,4D}$, are often used as useful figures of merit to characterize the photoinjectors. $B_{n,4D}$ is a function of the current I (peak or average) and the transverse emittances $\epsilon_{n,x}$, $\epsilon_{n,y}$;

$$B_{n,4D} \propto \frac{I}{\epsilon_{n,x}\epsilon_{n,y}} = \frac{qf}{\epsilon_{n,x}\epsilon_{n,y}} \tag{1.5}$$

at the bunch repetition rate f. Combining Eq. 1.4 and 1.5, the transverse beam brightness can be maximized by increasing $\mathrm{E_{cath}}$ and q and decreasing $\epsilon_{i,x}$ (or MTE) and kT.

1.1.2 Requirements

The attractive part of using electron sources for dynamic systems studies is that the apparatus can be much smaller than X-ray synchrotron sources, enabling tabletop experiments[24]. Along with 10^6 times greater scattering cross section of electrons, shorter temporal resolution (sub-ps) and less timing jitter makes the electron source even more appealing. However, the transverse coherence (or the spatial resolution) for x-ray sources such as XFELs is presently superior compared to electron diffraction using the available photoemission sources.

A photoemission electron source is made of two principal parts: a photocathode placed in an accelerating high-field environment. The photocathode is characterized by its cathode material choice, its corresponding photoemission physics, the initial electron rms beam size, the charge of the electron bunch and the resulting transverse coherence. The acceleration concerns the maximum electric field available at the cathode and the final electron energy out of the source.

An ideal cathode requires high quantum efficiency (QE) with a long lifetime for robustness operation. For a bright electron beam, low emittance (or low MTE) with sufficient bunch charge are among other key factors to consider. More specifically, the UED application needs long transverse coherence length $L_{c,x} \gtrsim 1$ nm, sufficient bunch charge $q \gtrsim 10^5$, and short pulses length $\sigma_t \lesssim 100$ fs [12, 24] and these parameters are closely interrelated:

$$L_{i,c,x} = \lambda\!\!\!^{-}_e \frac{\sigma_{i,x}}{\epsilon_{i,x}} = \sqrt{\frac{m_e c^2}{\mathrm{MTE}}} \tag{1.6}$$

$$\frac{L_{c,x}}{\lambda\!\!\!^{-}_e} = f_\epsilon \frac{\sigma_x}{\epsilon_{i,x}} \propto f_\epsilon \sigma_x \sqrt{\frac{m_e c^2}{\mathrm{MTE}}} \begin{cases} (E_{\mathrm{cath}}/q)^{1/2}, & \text{“pancake”} \\ E_{\mathrm{cath}}(\sigma_{i,t}/q)^{2/3}, & \text{“cigar”} \end{cases} \tag{1.7}$$

with the degree of emittance preservation $f_\epsilon \in (0, 1]$ and the reduced Compton wavelength of the electron $\lambda\!\!\!^{-}_e (= \hbar/m_e c = 3.862... \times 10^{-4}$ nm).

With the charge q fixed, the beam brightness $B_{n,4D}$ is proportional to the transverse coherence length $L_{c,x}$: a low intrinsic emittance $\epsilon_{i,x}$ and a high electric field E_{cath} are necessary, where low $\epsilon_{i,x}$ can be obtained by minimizing both $\sigma_{i,x}$ and MTE.

1.2 Bright Electron generation

Electron emission processes are mainly of three types: (i) field emission; (ii) thermionic emission; and (iii) photoemission. Field emission sources have been popular for electron microscopes and have advantages of long lifetime and easy maintenance.[25] Thermionic emission has been used for various applications including radiation therapy machines. Finally, photoemission electron sources are well known to produce bright beams with a short pulse duration. Each type has its own advantages and disadvantages, and there is no perfect way of generating electrons suitable for all applications. However, recent electron source

research has paid close attention to the photoemission guns as modern electron accelerators require high average current and ultra-low emittances[26]. Therefore, this thesis focuses on photoemission sources and low emittance cathodes for the bright beam production.

A photoemission process is determined by a cathode material and the incident laser wavelength. The cathode material has a given workfunction E_{work}, and the wavelength determines the photon energy $h\nu$, which determine the MTE, itself proportional to the excess energy $E_{ex} = h\nu - E_{work}$. In order to minimize MTE, the photon energy is chosen as close to the workfunction as practically possible. When the excess energy is close to zero, however, the QE decreases because these metrics are conflicting in terms of the cathode performance. Thus, trade-offs are necessary.

There are three types of photoemission materials suitable for low emittance beams: metal, semiconductor and cold atoms (see Fig. 1.2. The metal cathodes are least sensitive to vacuum and easier to introduce into photoemission guns than semiconductor cathodes, however, they typically require a UV laser and have a low QE. Semiconductor cathodes can be of two types: with positive electron affinity (PEA) and negative electron affinity (NEA). Electrons from these have high QE (up to tens of percent) when light in the visible range is used, but they are extremely demanding in terms of their vacuum requirements, down to 10^{-10} Torr. Also, the response time of the NEA type cathodes is on the order of picoseconds, which is too long for certain applications.[26] The cold atom sources tend to be limited by the number of electrons available in a bunch despite of their very low electron temperature ($\sim$ mK).[1, 27]

Electrons in cold and dense beams experience strong point-to-point Coulomb interactions soon after being emitted, called Disorder Induced Heating (DIH)[28]. This sets the theoretical limit to the electron temperature (kT_e), and MTE. Electron qualities for UED

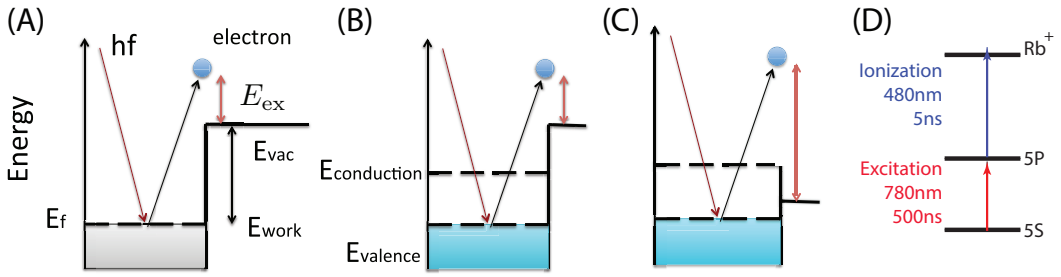

Figure 1.2: Photoemission process of (a) metal (b) semiconductor (PEA) (c) semiconductor (NEA) (d) cold atom[1]

are directly affected by DIH due to the charge and low emittance requirements. For example, ref[29] shows that the MTE of 5 meV is increased by 15 (32%) for 10^5 electrons (10^6), corresponding to electron densities of 4×10^{17} (4×10^{18} m^{-3}) . This changes the effective electron temperature from 60 K to 67 (77 K), corresponding MTE from 5 meV to 5.75 (6.6 meV). Electron beams with MTEs of 10 meV or less will be able to provide $L_{c,x}$ of 10's nm with a sub-ps time scale[29]. In comparison, cathodes commonly used today provide less than a $L_{c,x}$ 1 nm for otherwise comparable bunch parameters because their MTE's are in the range of 100 meV or bigger. Therefore, DIH affects the transverse coherence length severely for cold and dense electron beams.

1.3 Bright Electron beam control and transport

Apart from DIH, emittance growth mainly comes from non-linear effects. Non-linear space charge (SP) effects, the biggest contribution to the emittance degradation, can be taken

care of by shaping the laser pulse so that the emitted electrons near the cathode have linear fields.[30] SC effects can be suppressed with higher energies as γ^{-3}, which implies that a high gun voltage and accelerating gradient are generally necessary to minimize these effects.

In order to achieve femto-second electron bunches at the sample location, ultrashort laser pulses can be used along with a short electron propagation distance to the sample to avoid the space charge induced expansion of the bunch.[31] Otherwise, the electron beamline requires a bunch compression (an RF cavity) before the beam hits the sample. In this case, a laser with few pico-second pulse length can be used to reduce the emittance growth near the photocathode with superior brightness performance at the expense of increased complexity of the electron transport line.[16, 32–35]

Designing a bright photoemission source and its associated beamline requires detailed understanding of the space charge dominated beams. It involves trade-offs between many parameters, such as the initial pulse length, beam size, voltage, electric field, etc. An optimal solution is hard to find, however, the successful implementation of multiobjective genetic algorithms have demonstrated that the beamline elements can be optimized to obtain compelling beam quality for UED for realistically constrained parameters.[29]

1.4 Thesis outline

Having described the importance and challenges of bright electron beams for applications, particularly for ultrafast electron imaging, this thesis focuses on the development and construction of an ultra-bright DC HV photoemission electron source. Its three main scientific contributions include: demonstration of (i) cryogenically cooled photocathodes; (ii)

electron beam property differences between transmission and reflection mode photocathodes; and (iii) a cryogenic DC HV photogun.

Chapter §2 presents the development of ultra-low emittance diagnostics in order to prove the intrinsic emittance reduction by cryogenically cooling the multialkali antimonide photocathode near the emission threshold. The Transverse Energy meter (TEmeter) is designed to cool down the photocathode substrate to 90 K and generate electrons with up to 20 keV energy with a corresponding electric field of 4 MV/m. Near the photoemission threshold, photoelectrons have MTE of the substrate temperature so the MTE becomes ∼25 meV at RT and ∼8 meV at 90 K (among the coldest values ever measured for photocathodes up to date). Photocathodes with MTE below 100 meV have not been routinely studied and the corresponding measurement systems are not commonly available. This chapter demonstrates a simple and reliable tool to measure low MTE (below 100 meV) or equivalently, ultra-low emittance (<0.4 mm-mrad per mm rms laser spot) at photoinjector-comparable electric fields and at cryogenic temperatures. The Appendix A lists the sources of systemic errors in this apparatus.

Then Chapter §3 reports on the photoemission beam property differences of a Na_2KSb:Cs_3Sb photocathode for reflection and transmission modes. Operation of a transmission mode photocathode has a number of benefits over the commonly used reflection mode, e.g. the initial laser spot sizes ($\sim$ few μm) can be obtained by focusing the laser light using a very short focal length lens placed in the ultrahigh vacuum (UHV) environment of the gun just a few mm away from the back surface of the photocathode and shining the laser from the back of the cathode. Even with the advantages of the back illumination in the transmission mode cathodes, no previous studies have demonstrated the operation of alkali antimonide photocathodes in transmission mode nor compared their photoemission beam properties to those obtained from reflection mode operation. In this

chapter, the QE and MTE of a Na_2KSb:Cs_3Sb photocathode for reflection and transmission modes are provided along with analytical and numerical models of the electron transport and its effect on the photoemission parameters.

Finally Chapter §4 present a design of a compact electron photoemission source with a novel cooling scheme built at Cornell University. This electron source is designed building up on the results from the previous chapters and provides higher electric fields ($\sim$ 10MV/m) and lower temperatures ($\sim$ 40K) for ultra-bright electron beam production. This chapter is devoted to the design and commissioning of this photogun. Detailed descriptions of the surface treatment, the full thermal profile and HV conditioning data are provided. Photoelectrons with a maximum energy of 230 keV were successfully generated at RT and of 190 keV at cryogenic temperature. This gun will have a direct impact for bright electron sources development and their applications.

CHAPTER 2

Intrinsic emittance reduction in transmission mode photocathodes

This chapter was originally published as reference [19] .

2.1 abstract

This paper reports the development of a simple and reliable apparatus for measuring ultra-low emittance, or equivalently the mean transverse energy from cryogenically cooled photocathodes. The existing methods to measure ultra-low emittance from photocathodes are reviewed. Inspired by the available techniques, we have implemented two complementary methods, the waist scan and voltage scan, in one system giving consistent results. Additionally, this system is capable of measuring the emittance at electric fields comparable to those obtained in DC photoinjectors.

2.2 Introduction

The increased electron beam brightness from photocathodes enhances the performance of accelerators and enables new applications[8, 9, 36, 37] such as Free electron Lasers (FELs), Energy Recovery Linacs (ERL) and ultra fast electron diffraction (UED)[38]. Properties

like quantum efficiency (QE), mean transverse energy (MTE) or intrinsic emittance, response time and robustness are important figures of merit to determine the photocathode performance. The maximum possible transverse (two-dimensional) brightness B_n achieved from a photoinjector is determined by the MTE of the photocathode and the electric field at the cathode, E_{cath}[21] and is given by

$$\frac{B_n}{f}\Big|_{max} = \frac{m_e c^2 \epsilon_0 E_{cath}}{2\pi \mathrm{MTE}}, \tag{2.1}$$

where f is the repetition rate of the beam, m_e is the mass of an electron, c is the speed of light, ϵ_0 is the vacuum permittivity and MTE of is defined by

$$\mathrm{MTE} = \frac{1}{2} m_e \langle v_\perp^2 \rangle \tag{2.2}$$

with the transverse velocity $v_\perp$. In order to maximize the brightness, E_{cath} needs to be maximized and MTE needs to be minimized. As photoinjectors are required to operate at a high cathode field, it is essential to study the electron emission and measure the MTE at various electric fields comparable to the ones in real photoinjectors (several MV/m in DC photoinjectors and up to 100 MV/m in RF photoinjectors).

The MTE can be related to the normalized emittance $\epsilon_{n,x}$ of the beam at the cathode using the expression

$$\epsilon_{\mathrm{n,x}} = \sigma_x \sqrt{\frac{\mathrm{MTE}}{m_e c^2}}, \tag{2.3}$$

where σ_x is the rms size of the illuminated spot on the cathode[39] when there is no correlation between the position and the momentum on the phase space.

The MTE has been characterized experimentally[36, 39–41] and theoretically[42, 43] for various photocathodes. However, photocathodes with MTE below 100meV have not been routinely studied and the corresponding physics mechanisms oftentimes remain poorly

understood. We aim to build a simple and reliable tool to measure low MTE (below 100 meV) or equivalently, ultra-low emittance ($<$ 0.4mm-mrad per mm rms laser spot) at photoinjector-comparable electric fields and at cryogenic temperatures.

The organization of the paper is as follows. We first review and compare the available methods for measuring very low MTE electron beams. We then provide a detailed description of a device called the Transverse Energy Meter (TEmeter) developed at Cornell University photocathode laboratory to measure very low MTEs with two methods, the waist scan and the voltage scan. This design supports cooling of the photocathode from room temperature (300K) to cryogenic temperatures (90K). We also present a detailed systematic error analysis, which is essential in order to build reliable measurement apparatus. Finally, using the TEmeter we demonstrate the measurement of electron beams with MTEs as low as 22 $\pm$1meV from a cryo-cooled alkali antimony cathode.

2.3 Review of low emittance measurement systems

In this section, the review and comparison between currently available methods to measure very low MTE are discussed. Table.1 summarizes main available techniques.

The transverse energy spread can be inferred using hemispherical analyzers [2, 44] as well as time of flight (TOF) based detectors [45, 46] in Angle Resolved Photoemission Spectroscopy (ARPES) experiments. Fig. 2.1 shows a typical experimental configuration with a hemispherical analyzer.[2] Light with a photon energy larger than the work function of the material is incident on its surface. The emitted electrons are then collected by the hemispherical/TOF analyzer to give their energy and azimuthal/polar angular distributions. By rotating the sample stage, electrons from all angles can be obtained[46]. Such analyzers

Table 2.1: Comparison of existing methods

Method	Configuration	Disadvantage	lowest MTE measured
Hemispherical analyzer[2]	Differential voltage applied to sort energies	1) Sensitive to work function differences at low energies 2)not a direct measurement for emittance 3) sensitive to stray E/B fields 4) unreliable when measuring kinetic energy below 1eV 5) Cannot measure at fields greater than few V/m	$\sim$ 100 meV[44]
TOF analyzer[45, 46]	Delayed Line Detector to measure TOF and transverse position	1) a sub-ps laser pulse necessary 2) sensitive to stray E/B fields 3) unreliable when measuring kinetic energy below 1eV 4) Cannot measure at fields greater than few V/m	$\sim$ 130$\pm$5 meV[46]
Energy analyzer[3, 47]	Motion of electrons in longitudinal magnetic field	1) Cannot measure at fields greater than few V/m 2) strong magnetic field might affect photoemission	25$\pm$2.5 meV
E$\times$B technique [48, 49]	Crossed electric and magnetic field between the plates	Impractical to extract MTE information due to complex mathematical post-processing involved	N/A
Waist scan [36, 39, 39, 50, 51]	electron gun + a magnetic lens	careful magnetic field calibration required	$\sim$ 1 meV[36]
Beam sampling/ Pepper-pot [50, 52, 53]	two slits + a detector/ a slit + a detector	resolution comparable to the intrinsic emittance for low MTE beams	35 meV[54]
Free expansion[5]	acceleration + free expansion	1) laser diffraction 2) small laser spot required 3) grid non-uniformity	27 meV[5]
TESS[55]	free expansion in acceleration	1) small laser spot required 2) Cannot measure at fields greater than few kV/m	45$\pm$ 7meV[55]

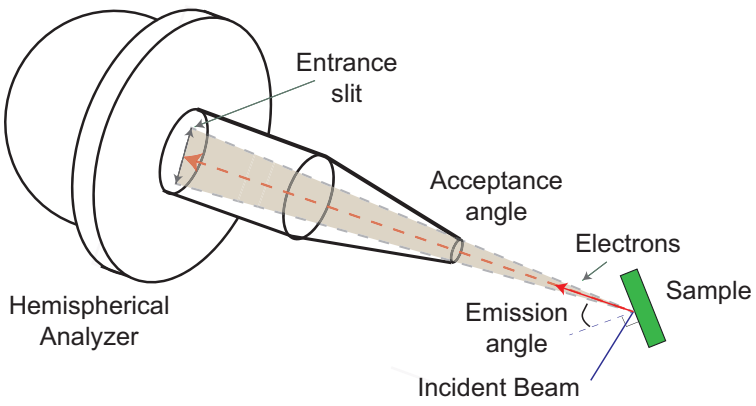

Figure 2.1: Hemispherical analyzer schematic for ARPES[2]

are designed to study the energy-momentum dispersion relationship in solids[2] and can map energy and angular distribution of emitted electrons from which it is possible to infer the MTE. The main issue to measure the low MTE electrons is that the analyzer is designed to deal with electrons emitted with a kinetic energy larger than a few eV. This limitation arises from the sensitivity of low energy electrons to stray magnetic fields and work function differences between the analyzer and the cathode. This limits the usefulness of these systems to studying the emission processes for higher (>eV) energy electrons.

Several other techniques exist to measure the MTE of low energy electrons by using strong electric or magnetic fields. Longitudinal and transverse energy distributions can be measured using the principle of adiabatic invariance and the motion of low energy electrons in a strong magnetic field[3, 47]. The configuration is shown in Fig. 2.2. A resolution of less than 6 meV rms in the energy distributions was demonstrated by this method[3]. MTEs as low as 25 $\pm$ 2.5 meV have been measured from GaAs photocathodes using this technique. However, this technique does not allow measurement of MTE under high electric fields. Thus, it cannot reproduce the conditions in an actual photoinjector and measure

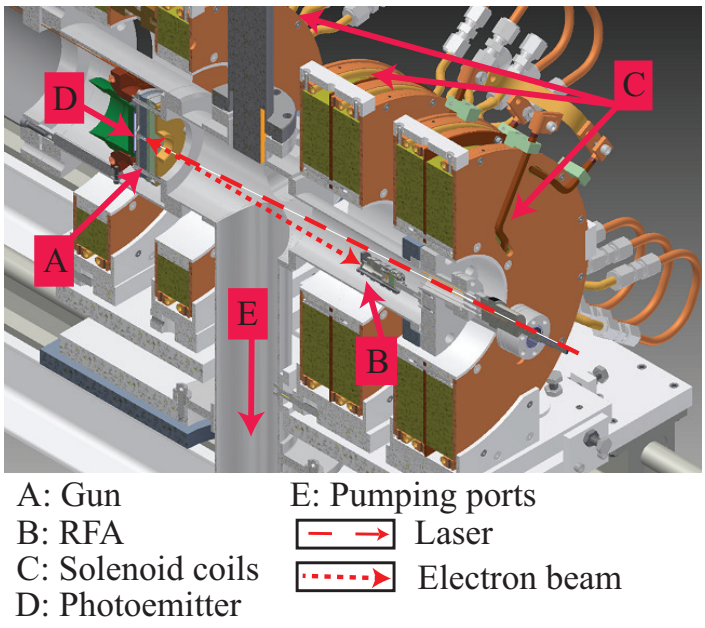

Figure 2.2: A section view of 2D energy analyzer. RFA is a acronym of retarding field analyzer. The details can be obtained in the reference[3].

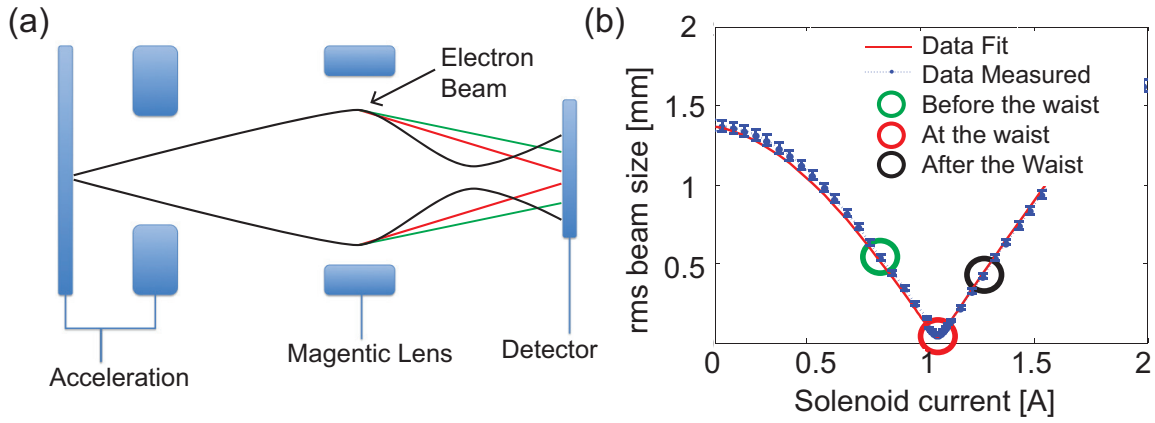

Figure 2.3: (a) Configuration of the waist scan. The magnetic lens has a variable focal length. The black, red and green lines represent the cases when the waist is before, at and after the scintillator screen respectively. The final rms beam sizes are measured as the current of the magnetic lens varies as shown in (b). The emittance is obtained from the least square fit based on the transport matrix. Each line in (a) corresponds to the colored circles in (b).

the dependence of MTE on the electric field. In addition to that, it is not understood how strong magnetic fields used in this setup would affect photoemission processes with ultra-low MTE.

Another method to measure a complete 3-D energy distribution by using crossed electric and magnetic fields was proposed.[48] However, retrieving the actual distribution from the measured photocurrents requires the use of complex Radon transforms[48], which is not practical. Due to this mathematical complexity, only 1-D distributions of polar angle and longitudinal energy have been separately obtained[49]. Hence this technique is not useful to measure the MTE.

Waist (or solenoid/quad) scan is one of the simplest and most common ways to measure the MTE in photoinjectors. This involves a magnetic lens such as a solenoid or a quadrupole, located in a drift region after an acceleration by an electric field. The schematic of the configuration is shown in Fig. 2.3(a). The electric field accelerates the electron beam to a relatively high energy. The focal length of the magnetic lens is varied by changing its current. This changes the electron beam envelope accordingly. The rms beam size at a certain distance away from the magnetic lens is measured using a scintillator screen followed by a CCD camera. For a particular electron energy, the spot size on the scintillator screen is recorded as a function of the current in the magnetic lens. The emittance of the beam at the photocathode and hence the MTE, can be deduced from these measurements if the linear transport matrices of the accelerating field and the focusing lens are known. When all the beam transport elements (accelerating field and the magnetic lens) behave linearly the electron trajectories can be modeled using a method similar to optical ray tracking. The linear transfer matrices $\mathbf{R} = \mathbf{R}_{i\rightarrow f}$ connect the initial profile of the beam

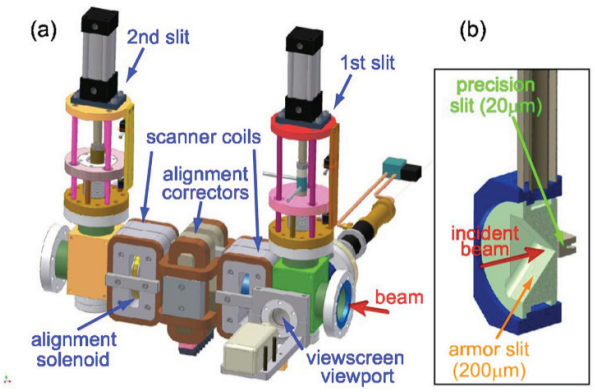

Figure 2.4: Two-slit emittance measurement system[4]

at the photocathode to the final profile on the scintillator screen as follows:

$$\begin{pmatrix} \sigma_x \\ \sigma_{\theta_x} \end{pmatrix}_f = \mathbf{R} \begin{pmatrix} \sigma_x \\ \sigma_{\theta_x} \end{pmatrix}_i \tag{2.4}$$

where the beam profile consists of its rms beam size, σ_x and divergence, σ_{θ_x}[56]. Detailed description about how to obtain the MTE from the spot size measurements can be found elsewhere.[39, 39] Various references[36, 39, 50, 51, 57] have shown studies of emittance measurements from diverse electron sources such as metal[51] and semiconductor photocathodes[39, 57] and ionized electrons trapped in a magneto-optical trap (MOT)[36]. Since this method strongly depends on the transport matrices and final beam sizes, extra attention needs to be paid to the precise modeling of each of the beam elements, nonlinear effects and the accuracy of the beam sizes. Exact measurements of the distances between the cathode, the anode, the focusing magnetic lens and scintillator screen and the electric and magnetic fields of the elements are necessary. Additionally, nonlinear effects such as aberrations and the space charge make it difficult to properly model this method and may even preclude its proper use. High resolution of detector and the CCD camera is also required.

Another popular way to measure the MTE in photoinjectors is a pepper pot or a beam

sampling technique[52]. The main advantage of beam sampling is that it allows mapping of the transverse phase space. In this method two slits are placed in the electron beam path to sample the beam where the slits are thick enough to stop the beam. The current of the beam so sampled is recorded. A schematic of this method is shown in Fig. 2.4. The first slit with the width d_1 selects the electron beam at the transverse position x away from the center of the beam. The selected electrons are then allowed to pass through a drift region. In the drift region, these electrons expand freely according to their transverse momentum spreads. The second slit with width d_2 is placed at the end of the drift region and only a few electrons which pass through the second slit are measured by a Faraday cup[53]. In order to obtain the entire phase space, scanner coils are used to sample the beam at various positions and transverse momenta. For a given energy of the beam, the resolution for this technique is limited by width of the two slits and the distance between them. Another variation of this method includes using one slit or a grid of small holes (called a "pepper pot"), and a screen instead of two slits[50, 58]. It is also possible to measure a time resolved phase-space by using a deflecting cavity in place of the Faraday cup[59]. At high energies, the slit becomes too thick so that it restricts the range of angles and also offers more opportunity to scatter. Although this method can map the entire transverse phase space and determine the emittance, the resolution of the phase space measurement can be comparable to the emittance obtained from the ultra-low MTE photocathodes making this technique inappropriate for the ultra-low emittance. Furthermore, this method inevitably involves interaction between slits and an electron beam. The contact of the electron beam with the slits can scatter the electrons and affect the MTE. While this effect may not be significant for the higher energy beam with a high MTE, it is not well understood how this method will affect a very low MTE beam.

The simplest method by far is to allow the beam to expand freely in an acceleration

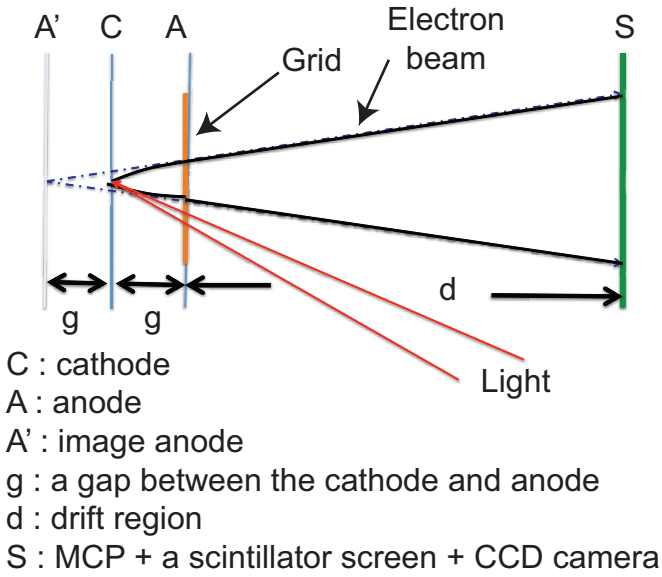

Figure 2.5: A schematic of free expansion technique[5].

and a drift region and obtain the MTE or the transverse energy distributions from the transverse size of the beam after the expansion[5, 55]. As shown in Fig. 2.5, an electron beam is generated from a small spot on the cathode (< 100 μm rms) using a focused laser. The electrons emitted experience a high gradient electric field between the cathode and the anode which is a fine electron microscope grid parallel to the cathode. The anode grid opening is small so that the defocusing due to the grid opening is negligible compared to the low MTE. The electron beam is accelerated only along its propagation direction. It passes through the grid and travels in a drift region to the scintillator screen where it is imaged. In the drift region the electron beam expands due to the transverse velocities of the electrons. The scintillator screen along with the micro channel plate (MCP) and a CCD camera obtains the image of the beam. The spot size on the scintillator screen is a function of the initial transverse energy of the beam, the voltage applied, a gap between the cathode and anode and the distance of the drift region.[5] Despite the simplicity of this technique,

much care is required to ensure that the the grid does not contribute to the measured MTE. The details regarding the grid contribution to systematic errors are given in Appendix A.

A variation of this configuration called transverse energy spread spectrometer (TESS) allows the beam to expand up to the anode. Instead of a grid the anode consists of the MCP and the scintillator screen. The beam spot is recorded on the anode itself.[55]. Given the voltage and the distance between the anode and the cathode, the image of the beam spread can be converted into the transverse momentum distribution and the MTE. This technique requires using a low ($\sim$100 V) voltage between the cathode and the anode in order to obtain a big enough spot size on the cathode. Hence this techniques is incapable of measuring MTE at high electric field gradients.

This review shows the advantages and disadvantages of each method. Considering the goal of measuring the low MTE from the photocathodes at photoinjector-comparable electric fields, the waist scan and the free expansion method are the simplest and the most reliable. The hemispherical analyzer, TOF spectroscopy and 2-D analyzer are unable to provide the MTE measurement at various electric fields and the crossed electric and magnetic field analyzer is only able to give the angular and longitudinal distribution of the emitted electrons. A pepper pot/beam sampling technique is limited by a spatial and momentum resolution from the configurations of the system.

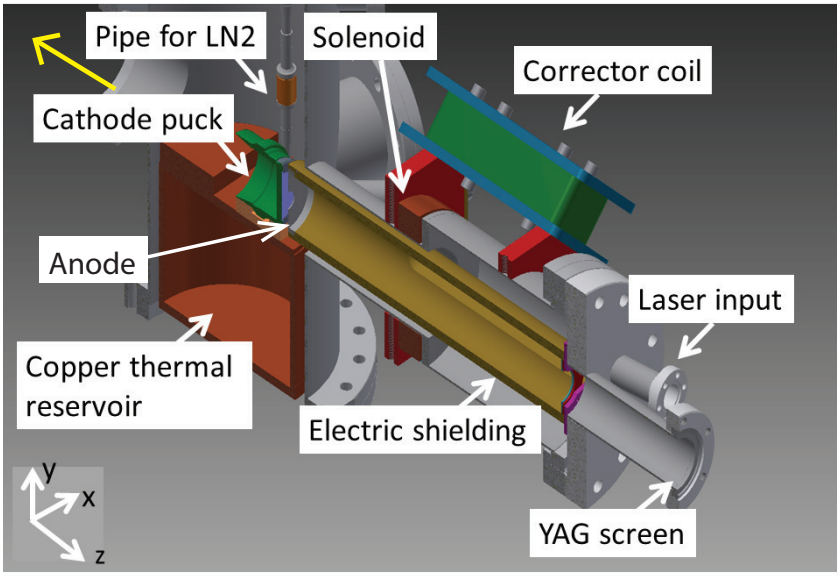

Figure 2.6: TEmeter chamber and beam line used in ultra-low emittance measurement. The beam moves toward positive z direction. The growth chamber is connected from negative z direction as the yellow arrow points out.

2.4 Demonstration of Cornell ultra-low emittance measurement

This section describe a system dedicated to measuring the ultra-low emittance of photocathodes with MTE below 100 meV. It includes a detailed description of the setup, measurement methods, analysis for error sources, and the results.

2.4.1 Description of TEmeter

The setup has been developed at the Cornell University Photocathode Lab and called the Transverse Energy meter (TEmeter). The photogun in TEmeter is capable of providing an electric field up to 3MV/m with a maximum voltage of 20kV. The system also has a

cryogenic system which cools the photocathode down to 90K. The schematic is shown in Fig. 2.6.

The cathode holder stays on top of a thermal reservoir made of a copper block, which can be cooled by liquid nitrogen (LN). The temperature of the cathode surface reaches 90 K in 2 hours once the copper reservoir is full of liquid nitrogen.

The TEmeter is connected to an alkali antimonide growth chamber via a UHV connection system with pressure in the sub 10^{-10} Torr range[60]. Alkali antimonide cathodes are grown on Si substrates on a circular stainless steel or molybdenum puck with 1 inch diameter in the growth chamber and transferred into the TEmeter. The vacuum in the TEmeter is 2×10^{-10} Torr.

The cathode along with the nitrogen reservoir are biased to a negative voltage while the anode is grounded. The cathode holder is designed so that the gap between the cathode and anode is approximately 5 mm. The exact gap can vary by $\pm$ 1 mm every time the cathode is inserted into the system. Therefore the gap is measured each time to determine the appropriate electric field map. The anode has a hole of 12 mm diameter and is held by a cylindrical electric field shield in order to minimize the stray electric field after the anode. Light passes through a pinhole, which is 1:1 imaged on the cathode using a set of convex lenses through an UHV window with about 6 degree angle with respect to the axis of the electron gun. The pinhole can be illuminated using a laser or the light from a monochromator. The photocurrent remains low to avoid space charge effects.

In the drift region, there is a solenoid and two sets of corrector coils. The corrector coils are used to cancel the effects of stray magnetic fields, including the earth's magnetic field, and to center the beam on the YAG screen. The corrector coils are wired in an aluminum mount and attached to the beam line.

The beam size on the YAG screen is measured by a charged-coupled device (CCD) camera connected to a computer. The CCD camera zooms in on the screen using a telescope so that a 11 μm/pixel resolution can be obtained. The initial beam size is measured using the telescope with a resolution of 27 μm/pixel.. The beam size on the cathode used the experiments are 60, 140, 170 μm which will be discussed in detail in section C.

2.4.2 Measurement methods

2.4.2.1 The waist scan

The waist scan follows the same principle as described in the references[39, 57]. It is important to remember that the waist scan method strongly depends on its measured rms beam sizes, especially sensitive near the beam waist. In this setup the final beam size varies from 1mm to 10μm, however, due to the limited CCD pixel size it is difficult to operate with one resolution to measure large variation of the beam sizes. This lead to taking the measurements with two different resolutions. The low resolution ($\sim$50 μm/pixel) captures the beam away from the waist and high resolution ($\sim$10 μm/pixel) measures the beam near the waist. When data taken by low and high resolution are combined, the most accurate emittance value can be obtained. Fig. 2.7 shows how combined resolution measurement produces the complete data set.

2.4.2.2 Voltage scan

This configuration does not rely on the solenoid and is close to the one for free expansion as mentioned before. The main difference between free expansion and voltage scan is the way each method obtain the emittance and MTE values. The free expansion converts the beam

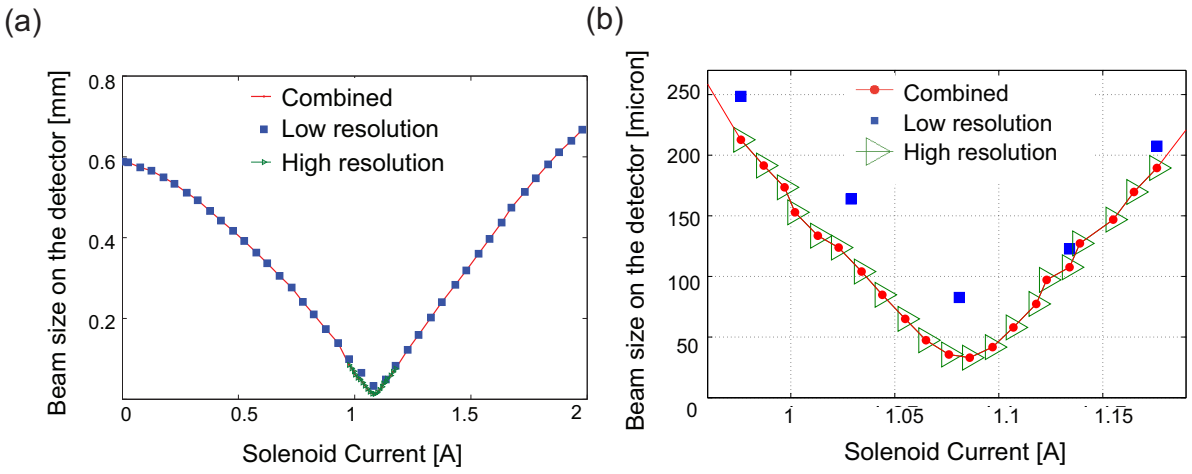

Figure 2.7: The solenoid scan works best when data from two different resolutions (11 μm/pixel and 45 μm/pixel) are combined. Figure (a) compares the data set for all resolutions. Figure (b) shows how high resolution captures its beam waist.

distribution on the screen at a given fixed voltage to the momentum in order to get the emittance and MTE. However, the voltage scan deduces the emittance from measurements of the rms beam size on the YAG screen at various voltages as shown in Fig. 4.6. The linear transport matrices can be constructed for the electric field generated by the cathode-anode configuration. This can be used to obtain the MTE from the rms beam size vs anode voltage curve using a least square fit as done in the waist scan method.

2.4.3 Error consideration for the TEmeter

In this section we discuss possible sources of errors in the MTE measurement described above. SUPERFISH[6] is used to generate the electric and magnetic field maps in the TEmeter and the General Particle Tracer (GPT)[61] is used to simulate the beam line of the TEmeter for both the waist scan and voltage scan configurations.

In the absence of space charge effects and non-linear beamline elements, the intrinsic emittance $\epsilon_{intrinsic}$ is preserved along the beam line. The beam current used for the

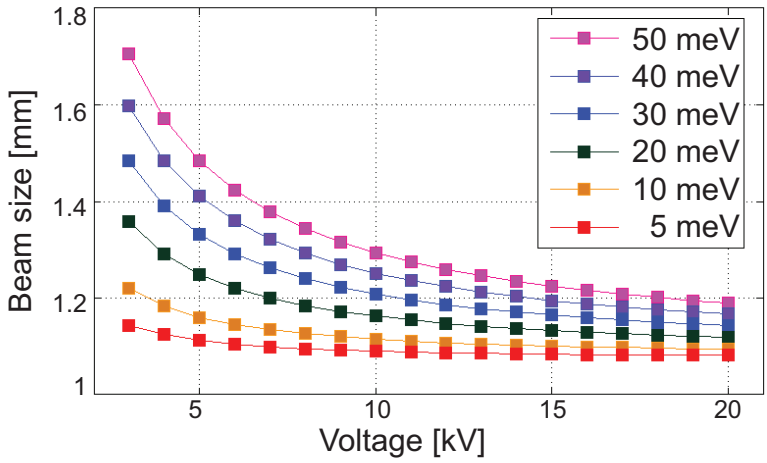

Figure 2.8: The rms beam size on the screen with respect to its beam energy for its initial MTE. The rms beam size on the cathode is 60 μm.

measurement in the TEmeter is small enough that space charge is not an issue. However, non-linearity in the anode and solenoid fields needs consideration. The emittance growth due to the non-linear fields can be assumed to be uncorrelated and the total measured emittance can be given by

$$\epsilon_{total} = \sqrt{\epsilon_{intrinsic}^2 + \epsilon_E^2 + \epsilon_B^2 + \epsilon_{B_{cath}}^2 + \epsilon_{others}^2} \tag{2.5}$$

where ϵ_E is the emittance growth due to the electric field aberration, ϵ_B is due to the magnetic field aberration, $\epsilon_{B_{cath}}$ is due to the magnetic field on the cathode and ϵ_{others} due to other factors like limited resolution while measuring the beam spot and mechanical vibration.

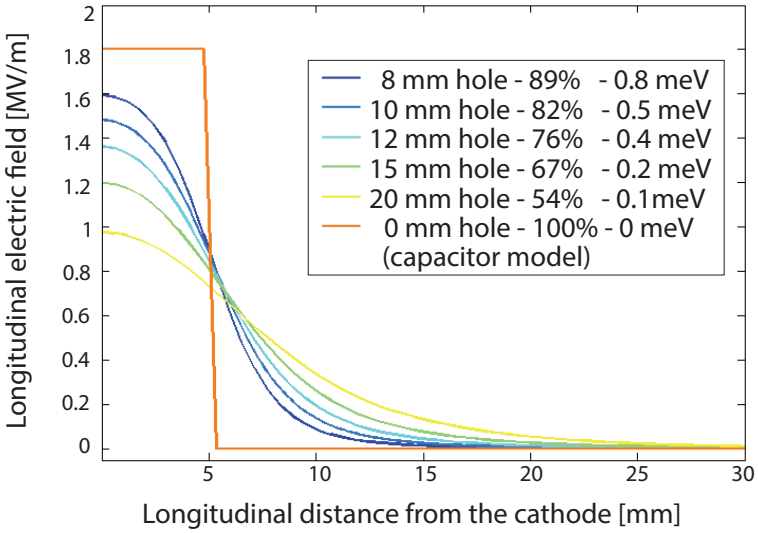

Figure 2.9: This figure shows the longitudinal electric fields for various hole sizes and relative field strength compared to the field for the capacitor model by using SUPERFISH[6]. It also provides the MTE gain for 500 μm initial beam on the cathode and zero intrinsic emittance.

2.4.3.1 Electric field aberration

The emittance growth due to the electric field aberration results from two main sources: an anode hole and a stray field. With proper design the effects of the stray fields can be minimized and ignored. The details regarding this are given in Appendix B.

In order to minimize the anode hole contribution an optimization of the anode hole size is required. A SUPERFISH[6] simulation is performed to calculate electric fields along the propagation axis and the MTE gain due to the emittance growth from the resulting aberration, see Fig. 2.9. As the hole size increases the emittance growth due to the anode aberration decreases, however, the electric field at the cathode also decreases. The emittance growth due to anode aberrations also increases with the size of the spot on the cathode and its offset from the center. In order to maintain the emittance growth below

5% for a initial spot size smaller than 200 μm and an offset of less that 100 μm and to obtain a strong enough electric field at the cathode, the anode hole size was chosen to be 12 mm in diameter.

2.4.3.2 Magnetic field aberration

The emittance growth due to the solenoid aberration can be calculated by

$$\epsilon_B = \frac{2\alpha\sigma_{xs}^3}{\beta\gamma}\sqrt{5x_0^2 + 2\sigma_{xs}^2} \tag{2.6}$$

where x_0 is the beam offset from the solenoid magnetic axis, σ_{xs} is the beam size in the solenoid and α is defined by

$$\alpha = \frac{1}{4}\Big(\frac{e}{2m_e c\beta\gamma}\Big)^2 \int \Big(\frac{\partial B}{\partial z}\Big)^2 \mathrm{d}z. \tag{2.7}$$

[30] Here β and γ are the relativistic factors. Since the emittance growth is proportional to the 4^{th} power of σ_{xs}, we use the smallest possible laser spot on the cathode. There may be an offset of up to 3 mm between the anode and the solenoid due to the mechanical design of the setup. With this offset and a MTE of less than 50 meV the beam size at the cathode should be smaller than 60 μm to keep the emittance growth below 5%.

2.4.3.3 Magnetic field on the cathode

When the electron beam is emitted from a cathode with a nonzero residual field B_z, it obtains an angular velocity that leads to emittance growth. The transverse momentum then becomes $\sigma_{p_\perp} = \gamma m \sigma_x \dot{\theta}$ where $\dot{\theta} = -\frac{eB_z}{2\gamma m}$. Since $\epsilon_{n,x} \sim \frac{\sigma_{p_\perp}}{mc}\sigma_x$, the growth is estimated by

$$\epsilon_{B_{cath}}[mm - mrad] \sim 0.3 B_z[mT]\sigma_x^2[mm] \tag{2.8}$$

[52] where σ_x is the spot size on the cathode. The magnetic field at the cathode is 0.23 mT when the solenoid current is set to 1 A. As the gun voltage increases to above 10kV, the

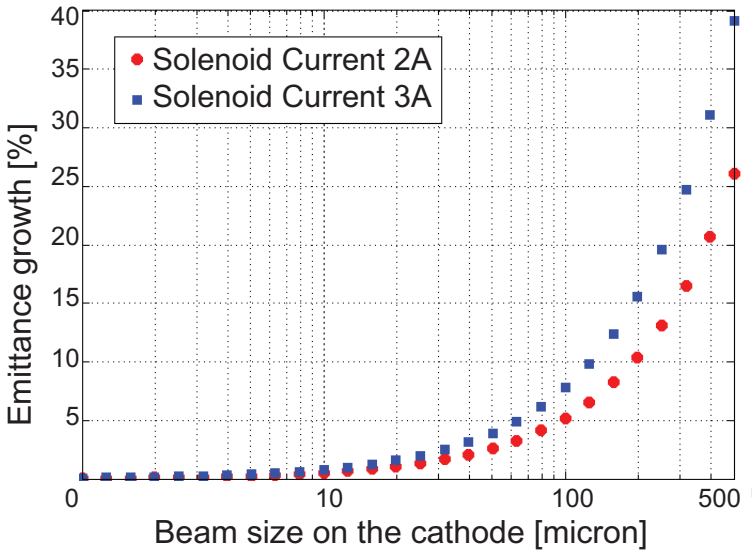

Figure 2.10: Emittance growth according to the initial beam sizes and solenoid currents with respect to its cathode intrinsic emittance for 30meV.

solenoid current for its waist gets larger than 2 Amps and the solenoid for measurement ranges up to 3 Amps. As shown in Fig. 2.10, the initial beam size on the cathode must be approximately 60 μm in order to avoid the emittance growth becoming greater than 5%.

2.4.3.4 Other possible error sources

Inaccurate measurement of the rms beam size on the scintillator screen will contribute to systematic errors in MTE. According to GPT simulations the waist size goes below 20 μm for a MTE of $\sim$30 meV for the voltage of 10 kV. A resolution of 11.3 μm/pixel is sufficient to measure this spot accurately. However, a better resolution will be required to measure smaller spot sizes. In order to maintain the spot size above 20μm rms, the voltage during the solenoid scan was kept below 10kV.

These methods depend strongly on the final rms beam sizes, so the reliability of the sizes on the detector is important. With high currents, there is a possibility of saturation

on the screen. When the electrons charge up the screen, the final beams may be distorted, negatively affecting the measurement. Another consideration is the thickness of the scintillator. A thicker scintillator can increase the amount of light produced but also add blurring. Instead, an MCP can be helpful for the very low current operation. It is necessary to ensure that the scintillator screen or MCP has a uniform sensitivity.

One should be aware that mechanical vibrations can contribute to the errors. The accurately measured beam sizes are a key requirement of this configuration. The spectrum of the vibrations is unknown and it is non-trivial to quantify the effect of vibrations and subtract its effect, particularly when the beam is tightly focused at its waist.

2.4.3.5 Requirements for measurements

The goal is to avoid having an emittance growth greater than 5% or having a systematic error in the MTE of 10%. For the voltage scan, the aberration due to the hole is negligible when the beam size at the cathode is smaller than 200 μm with an offset of 100 μm.

To limit the effect of magnetic field aberrations on waist scans, the rms beam size at the cathode must be less than 100μm. In addition the emittance growth due to the magnetic field on the cathode limits the beam size at the cathode to 60 μm and requires operating with solenoid currents less than 2 A. These requirements lead to operating voltages below 10 kV and an initial beam size of 60 μm.

2.4.4 The result

We performed ultra-low emittance measurements with both methods described above using a Cs_3Sb photocathode grown by co-deposition of Sb and Cs. For the solenoid scan with an

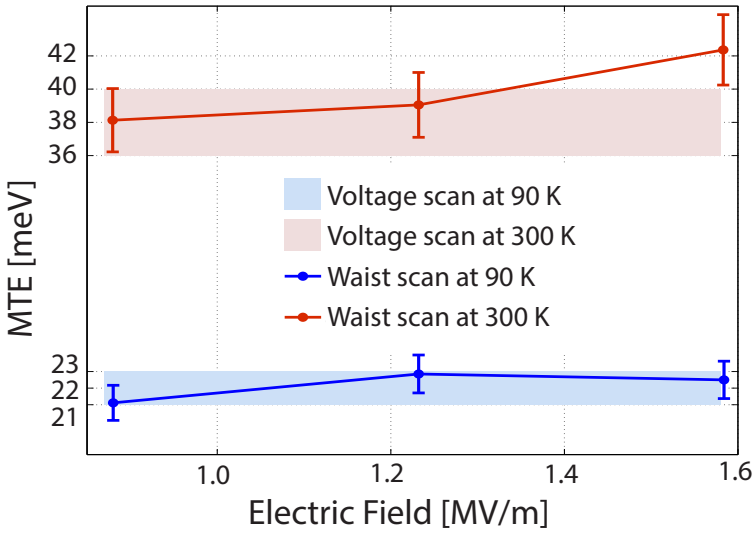

Figure 2.11: The MTE results obtained at 90K and 300K for the solenoid scan and voltage scan. The electric field intensities at the cathode surface for the voltage scan vary between 0.5 and 3.4 MV/m.

rms beam size at the cathode of 60 μm, the voltage was kept below 10 kV (equivalent to a 1.6MV/m electric field at the cathode).

The results obtained from the solenoid scan was found to be independent of the electric field at the cathode Fig. 2.11. This figure includes the voltage scan results and also shows that the MTE reduction from the ambient temperature (300K) to the cryogenic temperature of 90K.

Since the MTE obtained from the solenoid scan was found to be independent of the electric field at the cathode, the voltage scan could be performed to confirm the results obtained by the solenoid scan. Voltage scans with three different rms beam sizes (60, 140, 170μm) were also performed to obtain the same MTE as the solenoid scan. At the cryogenic temperature of 90 K, the MTE of 22 $\pm$ 1 meV was measured. The details of these results are in reference[20].

2.5 Summary

A compact device (TEmeter) that incorporates two independent techniques (the waist scan and the voltage scan) to measure low MTEs from photocathodes was developed. The TEmeter can not only measure photocathode MTE at high electric fields (comparable to those found in photoinjectors), but also measure MTE from cryogenically cooled photocathodes. The excellent agreement between the two techniques reinforces the validity of this measurement especially at small MTEs. It is possible to connect this tool to photocathode growth systems making it easy to characterize photocathodes and study photoemission physics under high electric fields.

Acknowledgement

This work has been funded by the National Science Foundation (Grant No. PHY-1416318). The authors would like to acknowledge the efforts of Dr. Xianghong Liu for the mechanical design of the TEmeter.

CHAPTER 3

Intrinsic emittance reduction in transmission mode photocathodes

This chapter was originally published as reference [62] .

3.1 Abstract

High quantum efficiency (QE) and low emittance electron beams provided by multi-alkali photocathodes make them of great interest for next generation high brightness photoinjectors. Spicer's three-step model well describes the photoemission process, however, some photocathode characteristics such as their thickness have not yet been completely exploited to further improve the brightness of the generated electron beams. In this work, we report on the emittance and QE of a multi-alkali photocathode grown onto a glass substrate operated in transmission and reflection modes at different photon energies. We observed a 20% reduction in the intrinsic emittance from the reflection to the transmission mode operation. This observation can be explained by inelastic electron-phonon scattering during electrons' transit towards the cathode surface. Due to this effect, we predict that thicker photocathode layers will further reduce the intrinsic emittance of electron beams generated by photocathodes operated in transmission mode.

3.2 Introduction

Alkali antimonides photocathodes[20, 63, 64] have already demonstrated their potential as photoelectron sources for the generation of high brightness beams for next generation light sources like Energy Recovery Linacs[65] and Free Electron Lasers[66]. When operated with photon energy close to their workfunction these photocathodes can provide electron beams suitable for ultrafast electron diffraction (UED) or ultrafast electron microscopy by having a lower emittance and higher QE's compared to those of metals[54]. Under the assumption of isotropic emission with no correlation between position and momentum the intrinsic emittance can be expressed as a function of the mean trasnsverse energy (MTE) of emitted electrons at the photocathode surface as $\epsilon_{i,x} = \sigma_x \sqrt{\langle p_x^2 \rangle}/m_e c = \sigma_x \sqrt{\mathrm{MTE}/m_e c^2}$ where $\epsilon_{i,x}$ is the rms normalized transverse emittance in the x-plane at the photocathode surface, σ_x is the rms laser spot size, $\langle p_x^2 \rangle$ is the transverse momentum variance, m_e is the electron mass, and c is the speed of light.

Photoemission has been usually described using the Spicer's three-step model[18]. Based on this model QE and intrinsic emittance of metal photocathodes have been predicted by approximating the Fermi-Dirac (FD) distribution with an Heaviside function and, thus, removing the dependence of these quantities on the actual electron gas temperature[40]. More recently, this model was extended to include the effects of a finite temperature of the electron gas, which allowed to explain experimental results for the photoemission excited when operated with photon energy close to their workfunction[7] indicating that MTE of photoelectrons is limited by the lattice temperature for both metals[5] and semiconductors[19, 20]. Electron photoemission is now predicted also for photons having energies lower than the metals workfunction or the sum of the energy gap and electron

affinity for semiconductors because of non-zero probability of having electrons with energy larger than the Fermi energy due to impurity and defect states localized in the energy gap.

This model initially developed for metal photocathodes operated in reflection mode does not include estimates of energy losses due to electron-phonon (e-ph) interactions assuming that electron-electron (e-e) scattering dominates over all the other relaxation channels and that any scattered electron will immediately lose enough energy that will not be emitted into vacuum. In the case of semiconductors the e-e scattering might not be the dominant relaxation channel because of the low free electron density in the conduction band. On the other hand electrons can then slowly relax through e-ph scattering losing a small amount of energy during each event. This effect is amplified the longer electrons have to travel in the material before the emission. Travel distances before emission can be increased by operating a photocathode in transmission mode. When the material extinction coefficient is much larger than the photocathode film thickness phoelectron are generated mostly near the substrate-photocathode interface or near photocathode-vacuum interface respectively for transmission and reflection mode as shown in Fig. 3.1(a). Becasuse the emission occurs at the photocathode-vacuum interface, electrons generated in the transmission mode must travel longer distances through the material before their emission resulting in smaller MTEs. The successful generation of electron bunches compatible with ultrafast electron diffraction for imaging of molecular and atomic motion requires sources capable of providing photoelectrons with extremely low MTE and a small initial laser beam size (on the order of several microns).[29] Generating laser spot sizes of few microns is a non-trivial task: photocathodes are usually operated in the reflection mode in high electric fields typical of high voltage DC or RF guns and the final lens of the optical imaging system for the laser to the photocathode surface cannot be located closer than some ten centimeters from the cathode surface itself.

Operation of a transmission mode GaAs-GaAsP photocathode with strained superlattice layers has been demonstrated for the production of a high brightness polarized electron beam[67, 68]. The electron gun energy was limited to 30 keV but the initial laser spot sizes smaller than 1 μm have been obtained by focusing the laser light using a very short focal length lens placed in the ultrahigh vacuum (UHV) environment of the gun a few mm away from the back surface of the photocathode[68]. Despite the attractiveness of operating photocathodes with back illumination in transmission mode, no previous studies ever demonstrated the operation of a transmission mode alkali antimonide photocathode in a modern photoinjector nor compared its photoemission properties with those obtained during reflection mode operation.

In this paper, we report on the QE and MTE of a Na_2KSb:Cs_3Sb photocathode for reflection and transmission modes, both performed on the same photocathode at different laser wavelengths. Analytical and numerical models of electron transport, which include e-ph scattering to account for the energy loss during electron's travel to the photocathode surface well reproduce the experimental data.

3.3 Measurement of transmission and reflection photocathodes

The Na_2KSb:Cs_3Sb was grown in a UHV chamber using vapors generated by effusion cells loaded with pure metals[69]. The energy band diagram of Na_2KSb:Cs_3Sb is shown in Fig. 3.1(c). In order to operate the photocathode also in transmission mode a 2.5 mm thick Borofloat 33 glass was used as a substrate. The electric contact between the glass surface where the photocathode film is grown, the retaining ring holding the substrate and to the

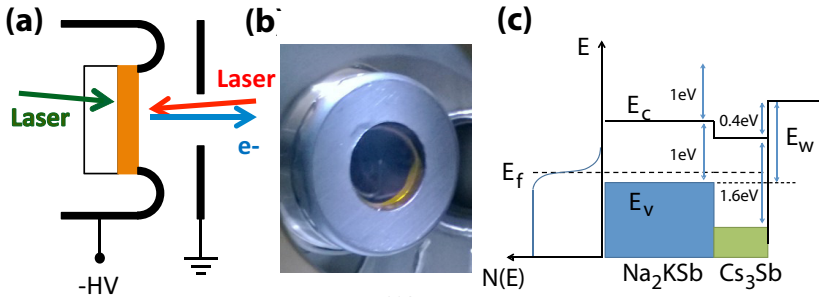

Figure 3.1: (a) Green arrow for light direction in transmission mode, red arrow for reflection mode. (b) A cathode puck with the metallic substrate holder. (c) Energy band diagram of Na_2KSb:Cs_3Sb photocathode. E_f: Fermi energy, E_v: Valence band maximum, E_c: Conduction band minimum, E_w: work function, which depends on the relative position of Fermi energies in the two materials

metal holder is ensured by small pieces of indium sheet metal soldering the border of the glass substrate and the ring. The metallic substrate holder is hollow allowing the transmission mode operation by passing light through the back of the substrate as shown in Fig. 3.1(b). A high voltage DC gun operated at 150, 200 and 250 kV was used in this experiment (with corresponding electric fields at the cathode surface ranging between 1.7 and 2.8 MV/m. A detailed description of the DC gun and the experimental beamline can be found elsewhere[70].

The solenoid scan technique was used to determine the emittance of the electron beam while operating the photogun with small laser diode modules and keeping the average photocurrent density sufficiently low (less than 0.1 μA/mm^2) so that space charge effects are negligible. The electron beam size is measured by means of a calibrated CCD camera imaging a BeO scintillator screen placed downstream of the solenoid and the gun as a function of the solenoid magnetic field. Linear optics transfer matrices from the cathode to the scintillator screen are used to solve a system of linear equations and retrieve the rms values of beam emittance and size at the photocathode. A detailed description of the method and measurement error propagation can be found elsewhere[36, 39, 56]. Three laser

apertures and three different gun voltages were used to verify the linear relationship between rms emittance value and rms spot size and to obtain intrinsic emittance as a function of the electric field. This method has already proven capable of ultra-low emittance measurements[19, 36]. Electron beam measurements have been performed using three different wavelengths chosen based on available diode lasers: 780, 690 and 532 nm. Two different optical systems were used to image the truncated Gaussian light distribution obtained with different size pinholes on the cathode surface. When the cathode was operated in transmission mode, a polished silicon wafer was used as a final mirror under UHV. The Si wafer was hosted on a UHV linear translator in the load lock chamber of the DC gun allowing to send the light to the back of the cathode.

The QE of the photocathode is obtained by measuring the photocurrent collected by a Faraday cup downstream of the gun using a picoammeter and by estimating the laser power incident on the photocathode surface using the laser power measured just before the last UHV window taking also into account all the transmission coefficient of the glass and the reflectivity of the UHV mirrors as a function of the different wavelengths. For the transmission mode cathode the transmission of the Borofloat 33 glass substrate (>95% in the 500-800 nm spectral range) has been included.

Photoelectrons' MTEs derived from the emittance measurements along with the QEs of the Na_2KSb:Cs_3Sb in transmission and reflection mode are reported in Fig. 3.2 and in Fig. 3.3 respectively. As anticipated, a consistent MTE decrease (about 20%, see Table 3.1) is observed when the cathode is operated in the transmission rather than the reflection mode for all the laser wavelengths used in the experiment.QEs were observed to slightly increase with the applied electric field (consistent with the Schottky barrier lowering due to increased electric field at the surface) while MTEs at each wavelength are the same within our measurement uncertainties. Our smallest measured intrinsic emittance is only $\sim 15\%$

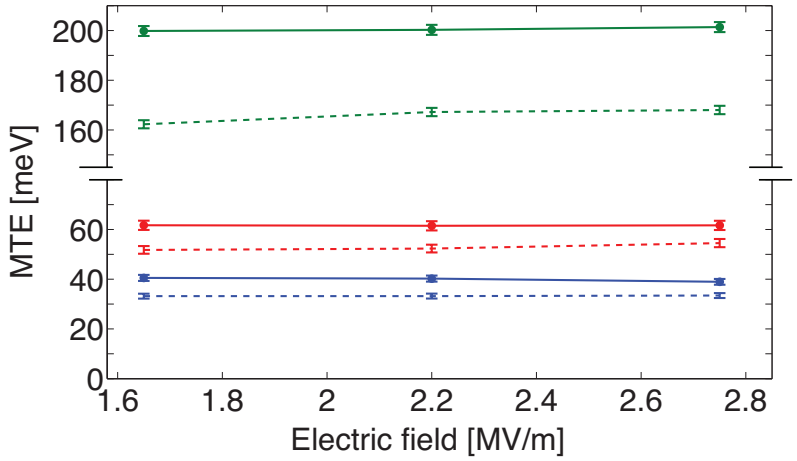

Figure 3.2: MTE measured as a function of electric field at the photocathode surface; green (532 nm, 2.33 eV), red (690 nm, 1.80 eV) and blue (780 nm, 1.5 eV); bold line represents the reflection mode; dotted line shows the transmission mode. Note the vertical scale.

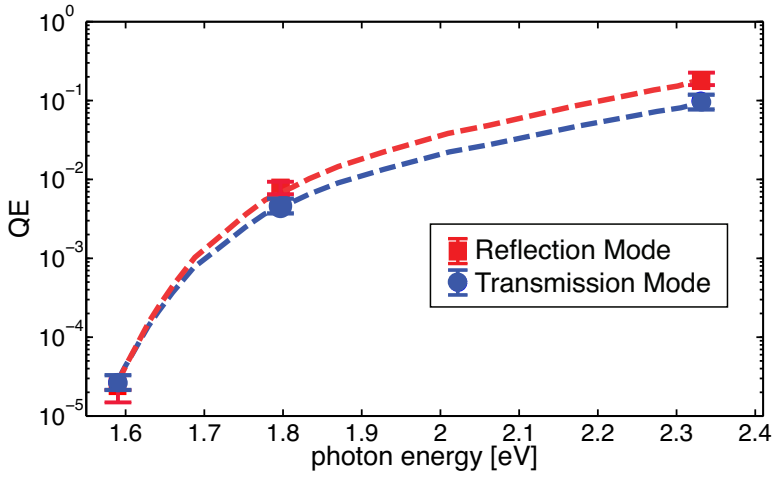

Figure 3.3: Quantum efficiency as a function of photon energy. The QE data at each wavelength are measured at 250 kV.

larger than the minimum value theoretically predicted. For these reasons we believe surface contributions to intrinsic emittance to be negligible.

3.4 Analysis: analytical solutions and monte-carlo simulations

In order to estimate the expected values of MTEs, we have derived analytical formulas using the Spicer's three-step model that also takes into account inelastic phonon scattering experienced by the electrons. The photon absorption is calculated from the complex index of refraction[71] assuming negligible absorption in the Cs_3Sb layer. The initial electron distribution is represented by an exponential decay function vs. the distance from the photocathode light-exposed surface. Electrons then have to drift towards the appropriate cathode interface in order to be extracted.

We obtain the following expressions for MTEs in the reflection and the transmission modes respectively:

$$\mathrm{MTE_{re}} = \frac{1}{3}\left[\mathrm{E_{ex}} - \frac{\overline{\mathrm{dE}}(\alpha - (\alpha+d)e^{-\frac{d}{\alpha}})}{l_{\mathrm{mfp}}(1-e^{-\frac{d}{\alpha}})}\right] \tag{3.1}$$

$$\mathrm{MTE_{tr}} = \frac{1}{3}\left[\mathrm{E_{ex}} - \frac{\overline{\mathrm{dE}}(d + \alpha(-1+e^{-\frac{d}{\alpha}}))}{l_{\mathrm{mfp}}(1-e^{-\frac{d}{\alpha}})}\right] \tag{3.2}$$

$$\mathrm{MTE_{tr}} - \mathrm{MTE_{re}} = \left[\frac{\overline{\mathrm{dE}}(-2\alpha + d + (2\alpha+d)e^{-\frac{d}{\alpha}})}{3l_{\mathrm{mfp}}(1-e^{-\frac{d}{\alpha}})}\right] \tag{3.3}$$

where $\mathrm{E_{ex}} = h\nu - \mathrm{E_w}$, $h\nu$ is the photon energy, $\mathrm{E_w}$ is work function, $\overline{\mathrm{dE}}$ is the average energy loss per collision, l_{mfp} is the mean free path of e-ph collisions, d is the thickness of the photocathode and α is the penetration depth of the photons. These expressions do not

take the finite temperature of the electron gas into account, but are useful to estimate photoelectrons' intrinsic emittance when excited far from the threshold.

Wavelength (nm)	Reflection (meV)	Transmission (meV)	Reduction (meV)
532	200±4	166±3	34±7
690	62±3	53±3	9±6
780	40±2	33±2	7±4

Table 3.1: Measured MTE for reflection and transmission modes at different laser wavelengths.

The mean free path of e-ph scattering events was calculated to be 25 nm using the rate reported in Ref. [72] and was assumed not to depend on the electron energy. A more complete treatment should include detailed estimates of scattering rates as a function of the electron energy for all possible scattering processes. These calculations fall beyond the main scope of this manuscript. Based on the measured deposition rates during the growth we estimated the thickness of the Na_2KSb being 150nm and the Cs_3Sb being few nm. For this reason we made the approximation that the effect of Cs_3Sb was only to lower the workfunction of the Na_2KSb and that photoemission processes arising from this very thin layer are otherwise insignificant. $\overline{dE}$ is assumed to be 22 meV as deduced from the measurements reported in Ref. [73]. MTEs resulting from these analytic formulas, Eqs. 3.1 and 3.3, are reported in Fig. 3.4 as a function of the photon wavelength.

The results obtained from the simple analytical model show that the electrons with reduced MTEs are expected from transmission-mode photocathodes, and that the thicker the photocathode layer is the larger the expected MTE decrease should be. However, this simple model fails as the photon energy approaches the emission threshold.

To include the effects due to finite temperature of the electron gas, a Monte-Carlo simulation was performed in order to better reproduce the measured MTEs near the

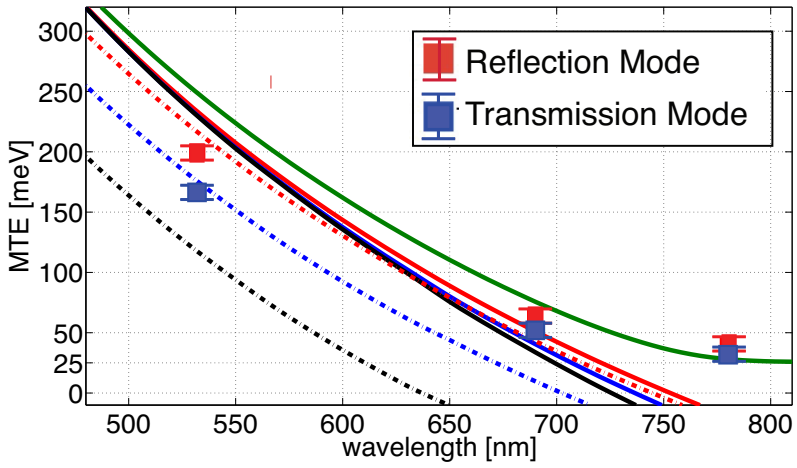

Figure 3.4: MTE from analytical formulas (Eq. 3.1 and 3.3) at three different photocathode thicknesses: 150(red), 300(blue) and 500(black) nm. Dotted lines represent the transmission mode. The green line is calculated with the model from Ref. [7]

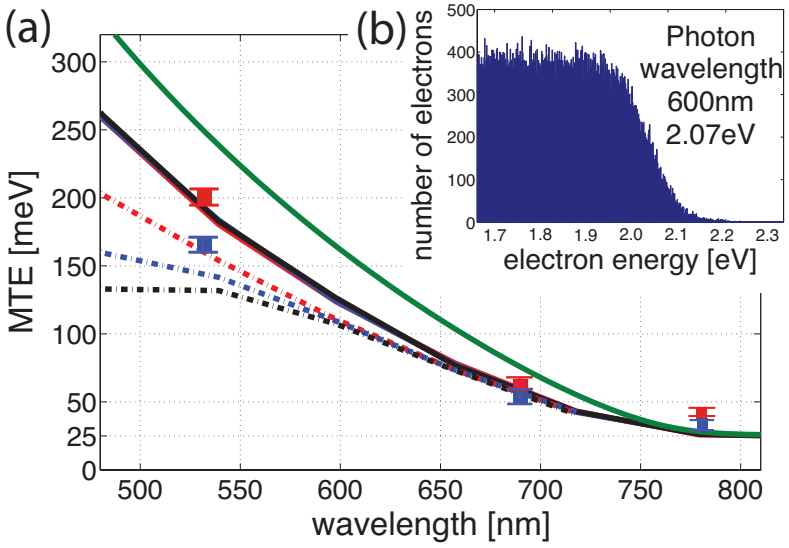

Figure 3.5: (a) MTE from Monte-Carlo simulations and experimental data as a function of laser wavelength. The color coding is the same as in Fig. 3.4. (b) A histogram of excited electrons above E_w following a FD distribution at room temperature.

emission threshold. Electrons were randomly generated as a function of the photon wavelength following a FD distribution. Inset in Fig. 3.5 shows an example of this distribution in energy. Electrons experience scattering events losing $\overline{\mathrm{dE}}$ for each collision. Path lengths x between successive collisions are randomly sampled based on a form of $e^{-x/l_{\mathrm{mfp}}}$[74]. Once an electron reaches the vacuum interface it is emitted if its longitudinal energy is larger than $\mathrm{E_w}$, see Fig. 3.1(c). MTE of the extracted electrons is then computed. The transverse energy is assumed to be conserved during the emission process. The results are shown in Fig. 3.5 for a value of $\mathrm{E_w}$=1.6 eV. An excellent agreement can be seen between the Monte-Carlo simulations that now include both e-ph scattering and the effect of finite temperature of the electron gas, which was missing from analytical formulas Eqs. 3.1 and 3.3. Note that a further reduction in MTE becomes very effective for transmission mode photocathodes via additional cryogenic cooling of the substrate[20].

The MTE reduction observed in these measurements can thus be explained by the increased number of inelastic e-ph scattering events when operating the photocathode in the transmission mode. The simulations also well explain why the absolute measured MTE lowers at longer laser wavelengths as the absorption coefficient gets smaller there. QE lowering up to 50% are measured in agreement with simulation when a 150 nm thick cathode is operated in transmission rather than reflection mode. Larger losses, up to 2 orders of magnitude, are expected from 500 nm thick cathodes.

3.5 Conclusion

In summary, we have reported in this letter on the measurement of electron beam MTEs and QE of a $\mathrm{Na_2KSb{:}Cs_3Sb}$ photocathode in a high voltage DC gun when operated in transmission and reflection modes respectively. We found that the MTEs generated from

the photocathode operated in the transmission mode is smaller by 20% in comparison with the reflection mode operation, which is accompanied by a corresponding QE decrease of about a factor of 2. We compared the measured MTEs with the analytical model and Monte-Carlo numerical simulations that include e-ph inelastic scattering experienced by electrons while drifting towards the vacuum interface. The analytic formulas and Monte-Carlo simulations support our explanation and predict that a thicker photocathode layer can be used to further reduce the intrinsic emittance via scattering events in the transmission mode photocathodes.

3.6 Acknowledgement

This work has been funded by the National Science Foundation (Grant No.PHY-1416318) and the Department of Energy (Grants No.DE-SC0014338 and No.DE-SC0011643).

CHAPTER 4

A cryogenically cooled high voltage DC photoemission electron source

This chapter is submitted in reference [75].

4.1 abstract

Linear electron accelerators and their applications such as ultrafast electron diffraction require compact high-brightness electron sources with high voltage and electric field at the photocathode to maximize the electron emission and minimize space-charge induced emittance growth. Achieving high brightness from a compact source is a challenging task because it involves an often-conflicting interplay between various requirements imposed by photoemission, acceleration, and beam dynamics. Here we present a new design for a compact electron DC high voltage (HV) gun with a novel cryogenic photocathode system and report on its construction and commissioning process. This photoemission gun can operate at ∼200 kV at both room temperature (RT) and cryogenic temperature (low T) with a corresponding electric field of 10 MV/m. It hosts a compact photocathode plug compatible with that used in several other laboratories opening the possibility of generating and characterizing electron beam from photocathodes developed at other institutions.

4.2 Introduction

Bright electron sources and their applications have become a critical area in accelerator science: Ultrafast Electron Diffraction (UED), for example, has benefited from the bright electrons used to observe ultrafast atomic-scale dynamics in tabletop setups. Yet in order to realize its full potential, single-shot UED demands longer coherence length and shorter bunch length at the sample location than what's available today.[11, 13–17] For example, among dynamic systems with various spatiotemporal scales, scientists are eager to study biomolecules such as proteins via UED to observe highly complicated atomic-scale motion exerting biological functions. Electron beams for these studies require long transverse coherence lengths $L_{c,x} \gtrsim 1$ nm, sufficient bunch charges $q \sim 10^5$, and short pulse lengths $\sigma_t \lesssim 100$ fs, [12, 24] confining electrons to a small 6D phase space volume. Among electron sources utilizing either photocathodes or cold atoms,[10, 19, 20, 33, 36, 54, 63, 64, 76] a high voltage DC gun with a suitable photocathode material of sufficiently small entrinsic emittance can potentially meet all these requirements.[19, 20, 29, 54]

For a given charge, the maximum achievable brightness highly depends on the mean transverse energy (MTE) of the emitted electrons and electric field. The transverse coherence length $L_{c,x}$, which sets the upper bound to the crystal unit cell size that could be imaged using UED setups, is closely related to the MTE[21, 29];

$$\epsilon_{i,x} = \sigma_{i,x}\sqrt{\frac{\mathrm{MTE}}{m_e c^2}}, \quad L_{i,c,x} = \lambda\!\!\!^{-}_e \frac{\sigma_{i,x}}{\epsilon_{i,x}} = \sqrt{\frac{m_e c^2}{\mathrm{MTE}}} \tag{4.1}$$

where $\epsilon_{i,x}$ is the rms normalized transverse emittance in the x-plane at the photocathode surface, $\sigma_{i,x}$ is the rms laser spot size,$m_e c^2$ is the electron rest mass, $L_{i,c,x}$ is the initial coherence length and $\lambda\!\!\!^{-}_e = \hbar/m_e c = 3.862...\times10^{-4}$ nm is the reduced Compton wavelength of the electron.

The electron beam in a small 6D phase space volume represents a challenge to emittance

preservation right from the moment of photoemission and through the propagation to the sample.[24, 77] Two main limiting phenomena to the achievable emittance can be identified: the so-called disorder induced heating[28, 78] and the space-charge effect[12, 77]. The transverse coherence length $L_{c,x}$ at a point of interest becomes a function of the electric field at the cathode E_0 and the charge q at the charge saturation limit, which can be written as:

$$\frac{L_{c,x}}{\lambda_e} \propto f_\epsilon \sigma_x \sqrt{\frac{m_e c^2}{\mathrm{MTE}}} \begin{cases} (E_0/q)^{1/2}, & \text{“pancake”} \\ E_0(\sigma_{i,t}/q)^{2/3}, & \text{“cigar”} \end{cases} \tag{4.2}$$

depending on the rms beam size $\sigma_{i,x}$, the laser pulse length $\sigma_{i,t}$, the degree of emittance preservation $f_\epsilon \in (0, 1]$ and the bunch shape (pancake vs. cigar-like).[21, 29] Note that we need to maximize E_0 and f_ϵ and minimize MTE to obtain longer $L_{c,x}$. The emittance can be both minimized and better preserved ($f_\epsilon \approx 1$) by increasing the applied voltage at the cathode,[77] at a given cathode-anode gap.[29] Additionally, our photocathode research has demonstrated that the intrinsic emittance near the emission threshold decreases from 0.27 μm/mm (or MTE of 38$\pm$2 meV) at 300K to 0.2 μm/mm (or 22$\pm$1 meV) at 90K.[19, 20] This points to a venue for obtaining smaller photocathode MTEs by cooling down the photocathode substrate to the low temperatures.

Scientists who study dynamical systems have been eager to perform experiments using a compact tabletop setup,[79, 80] where a DC electron accelerator becomes beneficial especially given its excellent vacuum performance required for high quantum efficiency photocathodes. For this reason we designed a new photoemission HV DC gun capable of operating at cryogenic temperatures that combines the illustrated advantages. To further support this choice, we have recently carried out simulations that have shown that such a novel photoemission gun should be able to generate bunches with enough electrons for a single-shot UED with a $\sigma_t \approx$100 fs and $L_{c,x} \gtrsim$ 30nm in a radius R = 200 μm spot at the sample assuming an initial MTE of 5 meV.[29]

In this paper, we detail the design of a compact electron photoemission source built at Cornell University which includes a novel cooling scheme. We describe its mechanical design and we report on HV performance and thermal measurements. Then we report on the surface treatment and the assembly process used to yield and keep the HV surfaces free from contaminants and particulates. In addition, we illustrate the mechanism used to transfer the photocathode from the cathode growth chamber that was used to obtain the first beams from this cryogenically cooled photogun. Finally, we mention the beamline that will allow to perform the beam diagnostics and the first UED experiment using this source.

4.3 Mechanical Design and Assembly of the gun

4.3.1 Mechanical Design

A schematic view of the gun is shown in Fig. 4.1. All parts are made of 304 stainless steel (SST) unless otherwise noted. The top half of the gun hosts the high voltage (HV) connection while the bottom half — the cryopump that cools and holds the photocathode down and maintains cryogenic temperature. The top half consists of a main vacuum chamber, a custom made six-way UHV cross, equipped with eight additional 2.75" vacuum ports. The main chamber is hosting the electrode shell and the HV inverted insulator. The inverted insulator was welded to a 10" vacuum flange which was installed from the top of the chamber. Six of the additional flanges are used to install viewports, the other two for an extractor gauge and a UHV right-angle valve. The latter is used to connect another vacuum system which includes a turbomolecular pump, an ion pump, a leak valve manifold for a slow vent/pump and a source of ultra-pure He used to perform high voltage processing.

The flange at the bottom of the main chamber is used for connecting to the cryogenic

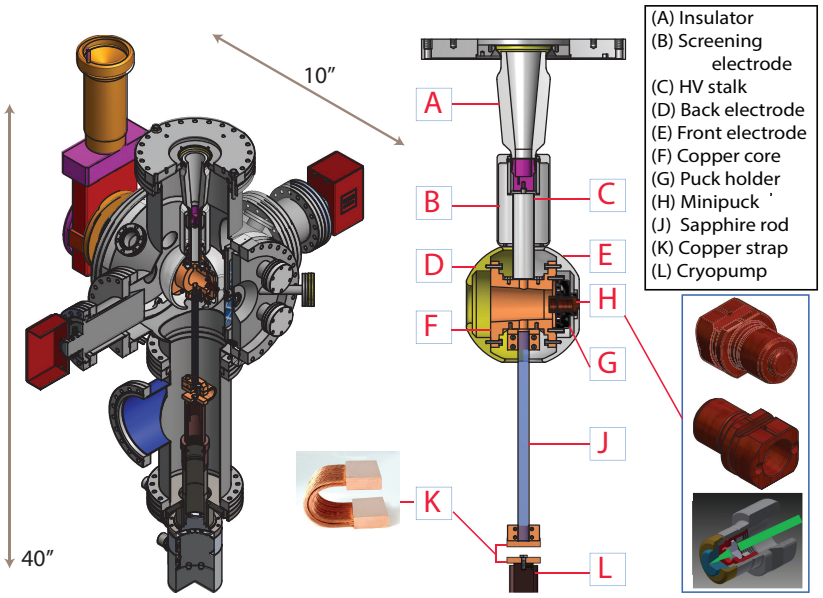

Figure 4.1: Left: A 3D model of the gun. Right: The internal structure of the gun. Inset: (H) The detailed view of the minipuck and the modified puck with a glass substrate and a focusing lens for transmission mode (bottom). The green arrow indicates a laser focused at the substrate.

system. Four non-evaporable getter (NEG) pump modules (H_2 pumping speed of 100 liter/s) as well as a 3" long beam pipe are installed on the front flange. A gate valve is connected to the beam pipe and is used to insulate the gun chamber from the rest of the beamline. Two ports equipped with a viewport each are also installed on the front flange allowing laser light illumination of the photocathode surface. The flange on the back of the gun hosts four viewports and a gate valve connected to a vacuum load-lock system designed to introduce photocathodes into the gun.

The inverted insulator (Fig. 4.1a) is a conical-shaped ceramic (Al_2O_3), whose vacuum-side surface is doped with a vendor-proprietary coating providing a low-level bulk conductivity. The resistance of the insulator was measured to be 16 GΩ, which will draw $\sim$14 μA at 225 kV. The receptacle side of the insulator hosts the HV cable (type R28 as specified by the length and angle of the receptacle). An HV stalk (Fig. 4.1c) is attached downward to

provide better mechanical support. It is shaped as a 100 mm long hollow tube with 0.5 mm thick walls co-axial with the insulator's center. A banana plug connector is installed on the bottom of the receptacle to electrically connect the cable to the HV stalk and electrodes.

Two electrodes are used in this gun: a screening electrode and a spherical shell electrode. The screening electrode (Fig. 4.1b) is a thin tube that shields the triple point junction, where the insulator, the HV stalk and vacuum come together. The thin tube also acts as a thermal shield reducing the thermal conduction from the insulator to the cryogenic electrode. The spherical shell electrode consists of two hemispheres, made of 316 SST vacuum remelt. These are joined and supported by an internal electrode structure. The front electrode (Fig. 4.1e) has a 2.5" diameter flat surface with a hole at the photocathode location (Fig. 4.1h) while the rear electrode has a 0.8" diameter opening to allow the cathode transfer. The internal electrode structure consists of two oxygen-free high thermal conductivity (OFHC) copper parts: a copper core (Fig. 4.1f) that connects the HV stalk to the cryogenic system and the puck holder (Fig. 4.1g) that holds the photocathode puck in place inside the spherical electrode.

The anode electrode is a grounded flat mesh (made with .0040 inch wire diameter placed in a grid with a spacing of 56 lines per inch) placed 20 mm away from the cathode plane and parallel to the flat surface of the spherical electrode. Two grid holders are used to secure the grid in place. They are bolted to the front main chamber flange but electrically insulated via ceramic spacers. The grid has two holes aligned with the front viewports allowing the incident laser beam to reach the cathode and the reflected light to exit the gun chamber. One last hole in the grid allows electron beam propagation out of the gun. The grid provides uniform electric fields in the cathode-anode gap region.

The bottom part of the gun assembly hosts the cryogenic system used for cooling down

the cathode electrode with the photocathode. It consists of a bottom UHV chamber and a cold source. The cold source is a cryocooler of the Gifford-McMahon type that is widely used for low-temperature systems. The cryocooler uses isothermal expansion of helium gas as a source to provide cooling to the cold finger (Fig. 4.1l). A compressor facilitates helium gas flow while a radiation shield is used to minimize radiation losses.

The in-vacuum thermal connection between the cryocooler and the copper core is made through a sapphire rod (Fig. 4.1j) and an OFHC flexible strap (Fig. 4.1k), to minimize the temperature rise thanks to their high thermal conductivities. The OFHC flexible strap (Technology Application, Inc.) is rated for a thermal resistance of 1.5 K per Watt and is installed on the cold finger to allow for thermal expansion and to minimize the transmission of vibration from the cryocooler to the cathode electrode.

The sapphire rod is cylinder 0.5" in diameter and 9" in length. Sapphire is well known for its superb thermal conductivity at cryogenic temperatures as well as its excellent dielectric properties[81]. Two copper pieces clamp the rod at each end connecting the rod to the internal electrode structure and to the copper strap. The space between the sapphire and the copper clamps is filled with 0.002" thin indium foils to facilitate and improve the thermal contact at each interface.

4.3.2 Assembly of the gun

One of the main challenges in operating a HV DC gun is in avoiding unwanted electric breakdowns at the design voltage. When electric breakdown occurs, the energy stored in the DC gun power supply is released in a very short period of time, which can cause a loss of the electron beam and degradation in the photocathode performance. Electron field emission is considered to be one of the main precursors of an electric breakdown.

Depending on the surface condition, electrons can tunnel from the solid to vacuum through the electrostatic barrier at the interface of a metal surface under a high electric field. Such unwanted field emission at the surface depends on its roughness and absorbed contaminants.[82] To minimize the probability of such events the following procedures were performed to prepare the relevant gun surfaces.

All UHV chambers and fittings were machined, leak-checked, and baked in air at 400°C for 5 days to minimize outgassing and reduce absorbed contaminants. Then, they were washed with detergent and water to remove grease, and ultrasonically cleaned. After being moved into a particle-free clean room, all surfaces were high-pressure rinsed with water to remove particulate contamination and then fully dried.

Three electrodes were mechanically hand-polished using fine sandpapers. Standard electropolishing was also performed to remove micro-scratches. Parts were stored under de-ionized water after mechanical polishing. The front electrode underwent an additional polishing procedure performed with diamond suspension of decreasing size (from 9 to 0.25 micron) and finished with alumina suspension of 0.05 micron. During assembly, the electrodes have been handled usig dedicated supports and the surfaces that were exposed to the high electric field gradient were never touched.

In addition to the careful preparation of the chamber and electrode surfaces, special care was taken to ensure cleanliness of all other vacuum components. For the mechanical assembly all tools were carefully cleaned before entering the clean room and whenever possible all the hardware components were washed with soap and water, ultrasonically cleaned and stored in double sealed plastic bags. Also silver coated copper gaskets were used to minimize dust particle formation during prolonged bake-out procedures. Whenever the gun was evacuated or vented, the speed of the air flow was limited to 200 standard

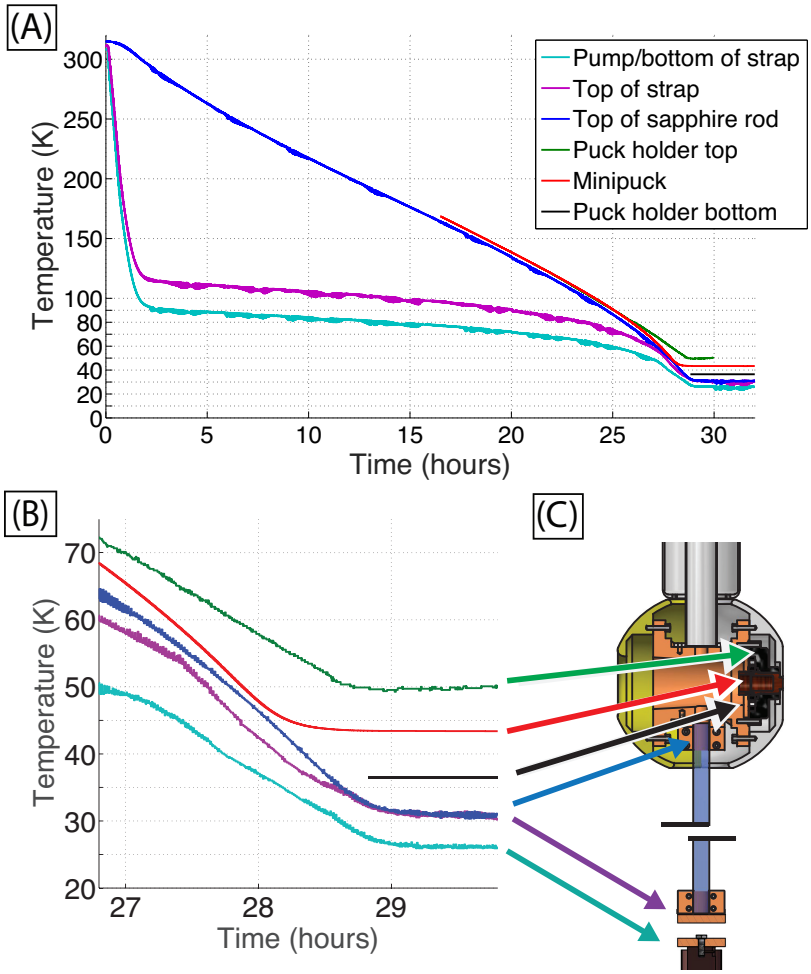

Figure 4.2: (A) Temperatures recorded during cooling down of the gun. (B) Temperatures near the thermal equilibrium. (C) Locations where thermal sensors were installed.

cubic centimeters per minute or less using a needle valve or a mass flow meter in order to avoid turbulent air flow transporting contaminants present in the system to critical locations.[83, 84] A bake-out of the vacuum vessel was performed at 120°C for three days and the six NEGs were activated during the bake-out. At the end of the bake-out the static vacuum level was approximately 2×10^{-11} Torr.

4.4 Thermal measurement and HV conditioning

4.4.1 Thermal measurement

The temperature profile, a critical parameter of this gun design, is shown in Fig. 4.2. Thermal sensors were attached from the internal electrode structure to the cryocooler, at several locations and their measurements are shown in Fig. 4.2c. The lowest temperature measured at the photocathode is 43±1 K after 29 hours of cooling.

We found that the thermal profiles and the achievable temperatures can be sensitive to changes of the surface roughness of the photocathode puck. Replacing an unpolished puck with one having the exposed surface polished to a mirror-like finish using diamond suspensions, allowed the cathode temperature to drop further by about 4K. Successive measurements reproduced the same initial and final temperatures, however, the required time for the system to reach a thermal equilibtium during the cooling increased from 22 to 30 hours. We speculate that some uncontrolled changes in the external radiation produced from the surfaces at ambient temperature might have influenced the cooling time. The temperatures of the puck holder (Fig. 4.2 green/black lines) were measured with type K thermocouples while temperatures at the other locations were measured using cryogenic-specific type sensors from Lake Shore Cryotronics, Inc. having an accuracy of 10 mK or better (corresponding to less than 100 mW heat load to the system). The largest temperature drop was located at the puck holder. From the top of the sapphire rod to the bottom of the puck holder the temperature changed from 29K to 35K and then again to 43K at the photocathode surface.

4.4.2 HV CONDITIONING

Electric breakdown represents a serious issue during beam operation. However, before a sustained and complete voltage breakdown happens due to arcing in the gun vacuum vessel, short arcing during a pre-breakdown event can lead to the annihilation of field emission sites allowing the electrodes to sustain higher voltages. In the absence of an electron beam generated from a cathode, pre-breakdown events are helpful to remove field emitters, preventing future breakdown eventually leading the gun strucuture to be stably operated at a desired voltage. This process is called "HV conditioning" or "HV processing".[82]

The gun is powered with a high-voltage power supply (HVPS) from Glassman High Voltage, Inc. capable of providing up to 320 kV. The HVPS is located in a custom-made chamber and is surrounded by 15 psi sulfur hexafluoride (SF_6) which is a commonly used dielectric gas to minimize arcing via absorbing free electrons.[85] The HVPS is connected to the gun using an HV cable and a processing resistor chain. The cable is an industrial x-ray HV cable type R28, which is rated up to 270 kV by the manufacturer, Dielectric Sciences, Inc. The processing resistor chain consists of fourty nine 4 MΩ resistors in series yielding a total resistance of 196 MΩ. The resistor chain prevents the gun from unwanted damage limiting the maximum current intensity during an arc.[70, 86]

The goal of the voltage processing is to minimize the number and intensity of electrons field emission sites at the operating voltage. At field emission locations uwanted electrons are extracted to the vacuum resulting in current flowing inside the gun in unwanted directions that can eventually produce high levels of radiation and/or gas desorption from the gun vessel chamber. Four radiation safety monitors were installed in the experimental room and are set to shut off the HVPS of the gun if radiation levels overcome the 2mR/h threshold. A vacuum level larger than 10^{-8} torr in the gun vessel or an excess current

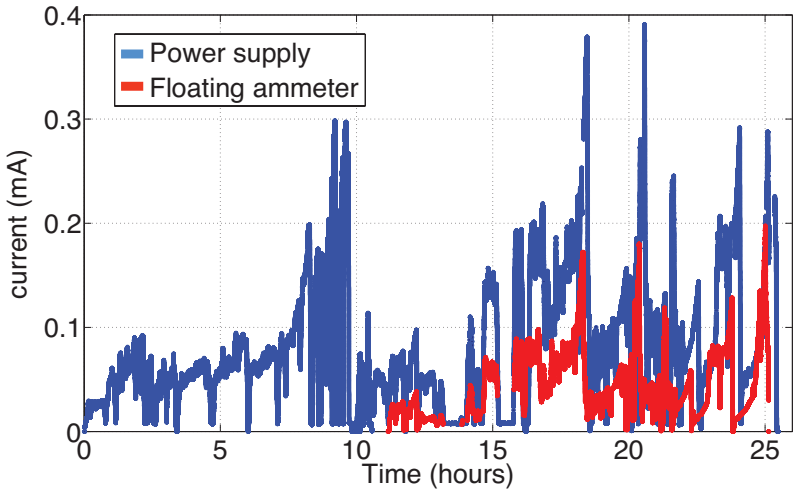

Figure 4.3: Electric currents drawn from the power supply (blue) and to the gun (red) as function of the gun voltage.

larger than 300 μA from the HVPS controller are also used as thresholds to turn off the HVPS to limit the gun activity before a major voltage breakdown. A pico-ammeter floating at the high voltage reads the current flowing from the processing resistor chain to the gun. A net excess current is defined as the difference between the currents from the floating ammeter and the current drawn by the insulator. To monitor the processing progress, the currents and the radiation levels are constantly recorded. The gun processing is performed until the gun activity (in terms of excess current, vacuum spikes, and radiation levels) are small enough or so diluted in time that they will not interfere with the beam operation at the desired gun voltage.

The gun processing was initially performed at room temperature (RT) and then again once the electrode was cooled down to the cryogenic temperature. The voltage applied to the gun was carefully increased while observing current and radiation activities as shown in Fig. 4.3 and 4.4. Within the first couple of hours we were able to quickly increase the gun voltage up to ∼150 kV. However, after this level several field emitter began producing

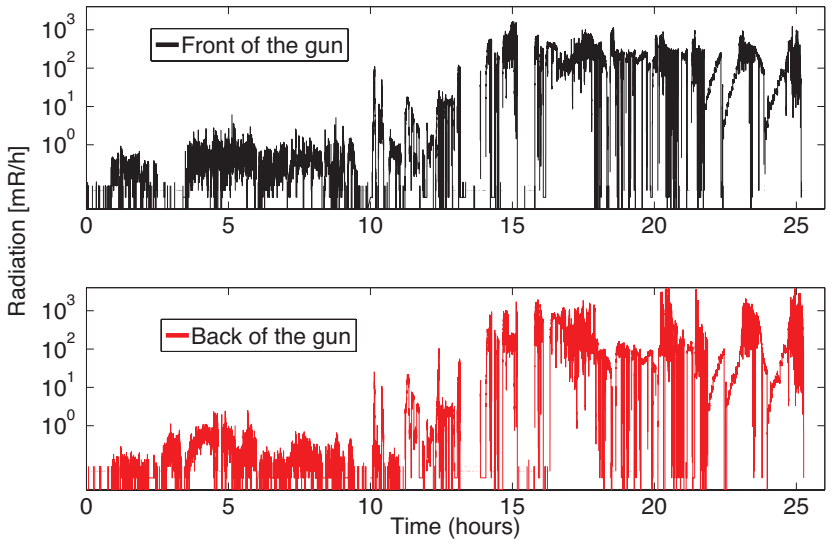

Figure 4.4: Intensity of radiation produced during the processing as measured near the front and near the back of the gun.

enough current and slowed down the conditioning process (Fig. 4.5). At this time high purity helium gas was introduced via a leak valve into the gun vessel until the vacuum level was increased above 10^{-5} torr with ion pumps off. The gun processing in low pressure of helium gas allowed the persistent field emitters to be removed and a voltage of ∼180 kV was achieved as shown in Fig. 4.5. Conditioning continued at RT for 11 hours alternating vaccum and He gas processing allowing an ultimate voltage of ∼270 kV to be achieved.

With the gun cryogenically cooled the voltage could be ramped above 200 kV without any issue as shown in black in Fig. 4.5. The goal for processing at cryogenic temperatures was to reach the operational voltage of 225 kV.[29] With continued processing the voltage reached almost 300 kV; however, the processing progress slowed down dramatically as compared to the rates obtained at RT. In principle, we could have used the gas processing to remove resistant emitters also at cryogenic temperatures but once gas is introduced at room temperature into the cooled gun at least 24 hours were required to completely cool

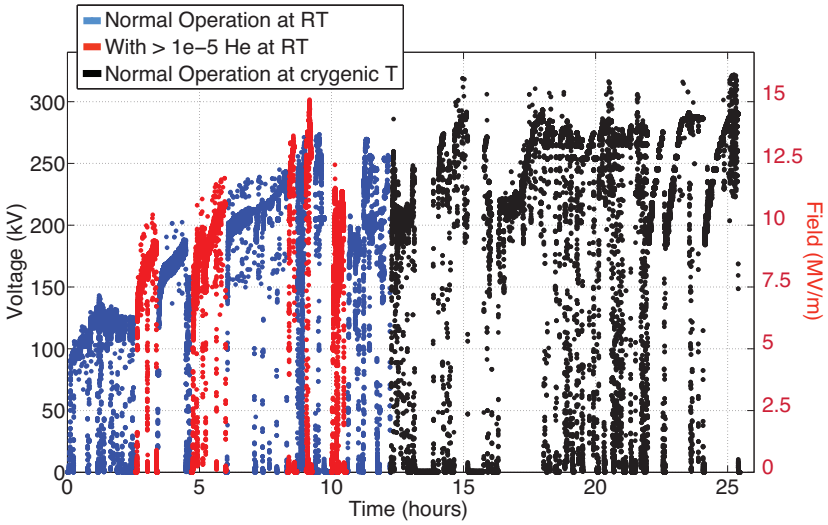

Figure 4.5: The voltage applied to the gun during the HV processing. The scale on the right side (red) reports the electric field corresponding to the applied voltage.

down the gun. Because this process was deemed as time expensive and we were already close to achieving the desired operating point, the gas processing was not used at cryogenic temperatures. After achieving the electric field gradients beyond 10 MV/m, we observed new field emitters appearing almost as frequently as the old ones were removed. This resulted in a gun voltage pattern with large fluctuations as seen in Fig. 4.5.

After approximately 22 hours of conditioning, the gun became stable near 225 kV. Fig. 4.6 shows the measured excess current and radiation levels as a function of applied voltage and electric field. Near the desired operation voltage, the gun draws approximately 2 μA of excess current and produces 10 mR/h of radiation just outside of the gun chamber. A BeO scintillator screen, placed along the beam line $\sim$37 cm away from the cathode surface, was also monitored with a CCD camera but no signs of field emitted electrons traveling into the beamline could be detected. At this stage we declared that sufficient gun performance was achieved to warrant an attempt to produce a photoelectron beam.

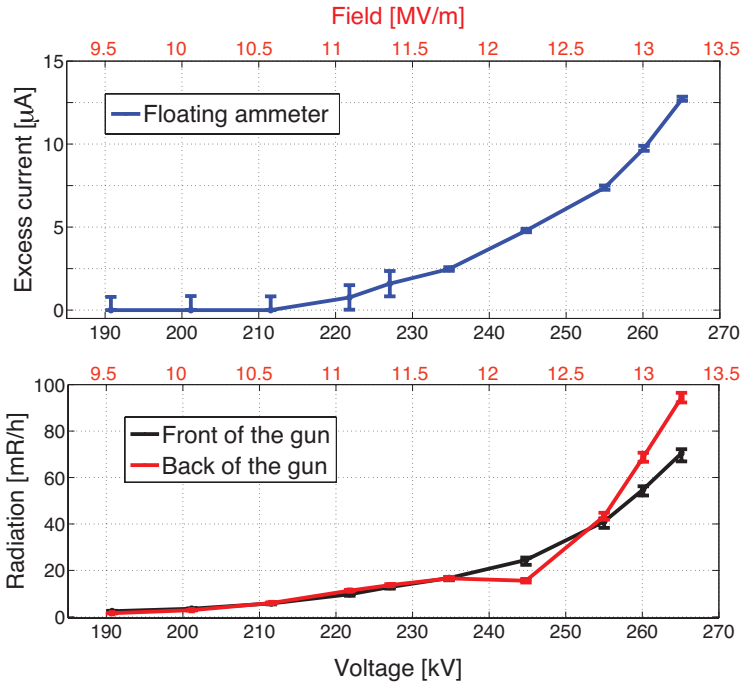

Figure 4.6: Gun performance data at cryogenic temperature at measured at different gun voltages (black labeled on the x-axis, in red the relative electric field intensities at the photocathode surface). Top: Excess current data. The excess current is defined as the difference between the current measured from the floating ammeter and the current drawn from the insulator (16 GΩ). Bottom: Radiation levels as measured near the front and near back of the gun.

4.5 Beam generation and Operation

4.5.1 Photocathode transfer and first beam generation

To generate the first beam a Cs_3Sb photocathode was grown on a minipuck suitableto be inserted into the cathode electrode (Fig. 4.1h). The Cornell University photocathode lab used to host thin film growth system that could only use a two inch puck like the one described in Ref. [54] and [53]. Thus, in order to utilize the existing facility an adaptor puck was designed as shown in Fig. 4.7i.[69] Two screws with spring-loaded spheres are used to secure the minipuck in place and two dowel pins to the minipuck within the adaptor.

After the cathode is grown, the adaptor (Fig. 4.7(I)) is moved into an exchange chamber (shown in top of Fig. 4.7) using a magnetic translator arm (Fig. 4.7a) under UHV conditions. The exchange chamber is designed to allow disengaging the minipuck from the adaptor and to move it into one of the cathode carriage slot. The carriage can then be moved using a vacuum suitcase to the gun location where the cathodes will be used. To perform the transfer first the adaptor is made to rest on the saddle in the holder assembly, then the saddle is shifted upwards using a UHV bellow linear translator (Fig. 4.7b) until the top flat surface of the adaptor align and touch the top side of the holder. Now the adaptor is firmly held in place by the holder assembly. The translator arm (Fig. 4.7a) can be now detached from the adaptor allowing the holder assembly to move further. A vertical translator (Fig. 4.7c) is used to move the holder assembly and the adaptor upward until they align with a minipuck gripper (Fig. 4.7d). The gripper grabs the minipuck and pulls it out while the adaptor is held in place by the holder. Then the holder assembly is lowered and the gripper is used to insert the minipuck into a slot in the cathode carriage (a side view of the carriege is detailed in the inset of Fig. 4.7). A magnetic arm equipped with a bayonet stile

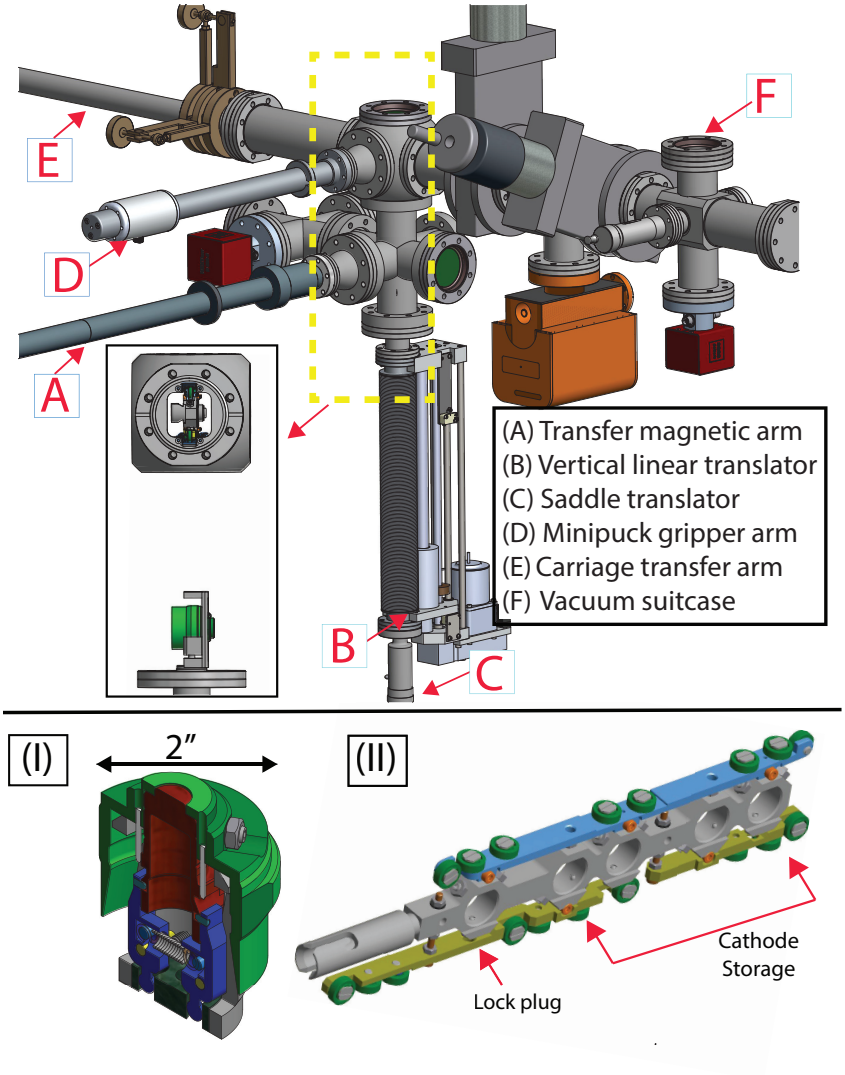

Figure 4.7: Top: Exchange chamber connected to the photocathode growth chamber. Bottom: (I) The assembly shows the minipuck (red), the adaptor (green) and the minipuck gripper (blue), and (II) the cathode carriage for the minipucks. The far left slot in the carriage is used to plug the lock during transportation in the vacuum suitcase.

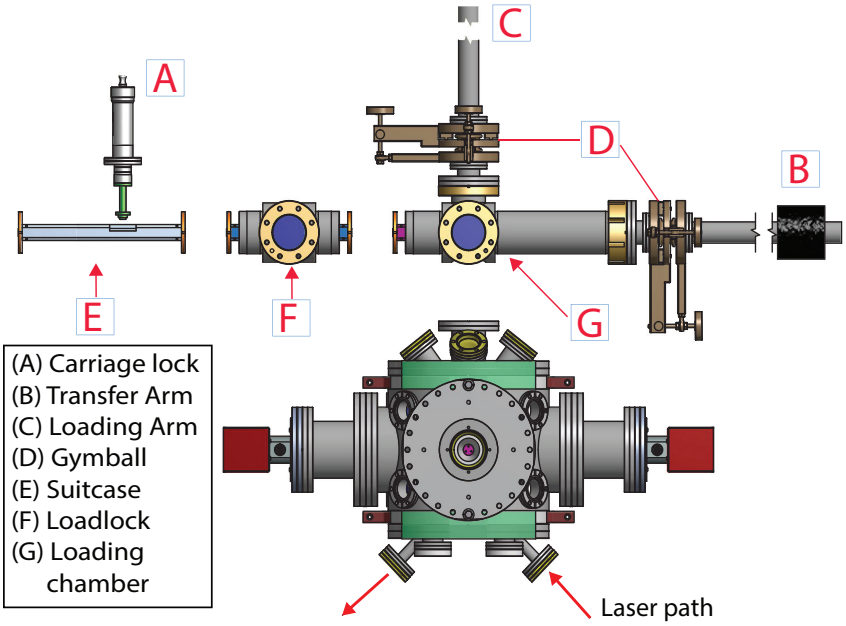

Figure 4.8: A top view of the cathode loading system used in the gun.

tip (Fig. 4.7e) engage the carriage that can hold up to four INFN/DESY/LBNL-type pucks and move it into a vacuum suitcase (Fig. 4.7f).

In the vacuum suitcase an insertable lock (Fig. 4.8a) prevents unwanted movement of the carriage engaging into the far left hole. The suitcase (Fig. 4.8e/Fig. 4.7f) is then transferred to the gun and attached to the loadlock chamber (Fig. 4.8f). A magnetic arm (Fig. 4.8b) engages and pulls the carriage into the gun loading chamber and a minipuck gripper (Fig. 4.8c) grabs a minipuck in the same way as in the exchange chamber. Two gimbals (Fig. 4.8d) are used to accurately align the translators (Fig. 4.8b/c). The gripper on the rear of the gun transfers the puck to the gun chamber and secures it to the puck holder. If the puck is properly engaged into the cathode electrode, the cathode surface can be seen from one of the laser view ports. Based on our previous measurements at least 30 hours are allowed for the electrode and photocathode to cool down and reach the thermal equilibrium.

Light from a supercontinuum tunable laser (NKT Photonics EXB-6 coupled with a

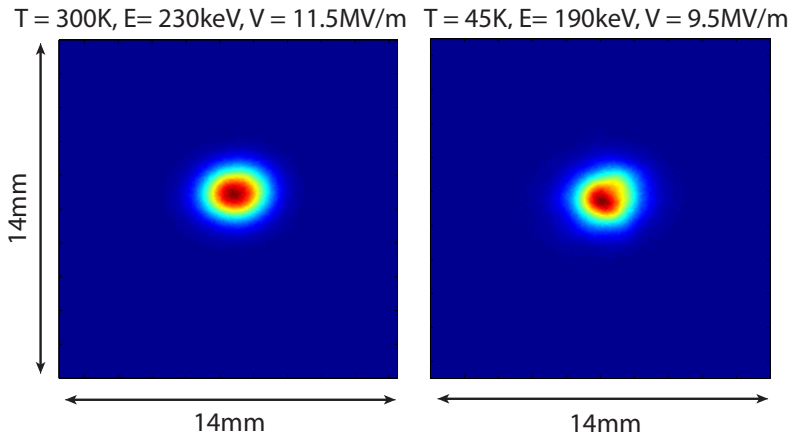

Figure 4.9: Electron beam images as collected by the CCD camera during operation at RT (left) and at cryogenic temperature (right).

NKT Varia filter with a 10 nm bandpass) enters one of the viewports connected to the front flange of the gun and shines on the center of the cathode. Photoelectrons are generated using photons with a central wavelegnth of 532 nm and accelerated under an applied voltage of 230 kV and 190 kV at RT and at cryogenic temperature (43K at the cathode) respectively. Electron beams were imaged using a BeO fluorescent screen placed ∼37 cm away from the cathode and the image captured by a CCD camera are shown in Fig. 4.9.

4.5.2 Beamline

The layout of the electron beamline designed to be operated with the Cornell Cryogenic DC gun is shown in Fig. 4.10. The beamline is divided into two sections before and after the UED sample chamber: the section before the sample chamber is designed to transport the beam to perform UED experiments and the section after the chamber is designed to perform the beam characterization. Just after the gun two identical solenoids[70] and a 3.0 GHz normal conducting buncher cavity whose design is based on Ref. [16]]are installed. These elements are used to control and manipulate the transverse size of the electron

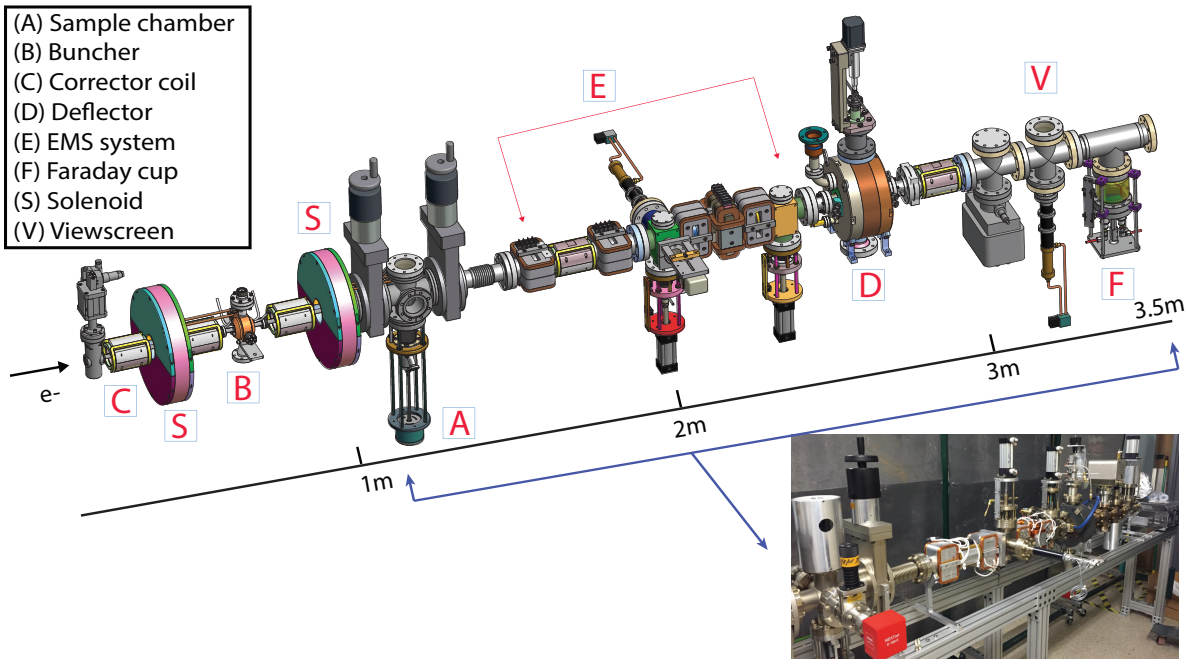

Figure 4.10: 3D model of the beamline of the Cornell Cryogenic DC gun. The electron beam propagates from the upstream of the gatevalve. Inset: The picture of the beam line.

beam and to compress the electron bunch duration at the sample chamber for the UED experiment. This configuration, with two solenoid and a buncher, has been used as model to perform numerical simulations aimed at optimizing the beamline characteristics using multi-objective algorithm.[29] The sample chamber can host a retractable scintillator screen to image the electron beam when the UED sample is not mounted.

The second half of the beamline is composed of the Emittance Measurement System (EMS), a 1.3 GHz deflector cavity, a scintillator screen (BeO) and a Faraday cup. The EMS is used to map the full 2-D vertical phase space density and consists of two retractable horizontal slits and two vertical kicker magnets. Slits and magnets are used to select electron with defined position and transverse momentum. Those electrons are collected by the Faraday cup and a picoammeter or a charge integrator are used to measure the collected charge or current and hence to reconstruct the transverse phase space of the

beam.[87] The deflector cavity is used to measure the bunch length of the electron beam. It applies a time dependent magnetic field to the electron bunch so that a correlation between the vertical coordinate and the time become correlated. The image of the beam on the scintillator screen can then be used to calculate the bunch length.[88] The same screen can also be used to measure the beam emittance using the method of the waist scan.[39, 56]

4.6 Future work and Conclusions

Photoelectron beams from Cs_3Sb photocathode have been demonstrated at RT and cryogenic temperature up to 230kV with a new type of electron gun. The photocathode puck holder (Fig. 4.1h) will be modified and replaced to reduce the stiffness of the spring-loaded mechanism used in the puck loading system (this will require opening the gun to air and reassembling the entire electrode structure in a clean room). A vacuum bake-out and an additional HV conditioning are expected to bring the photogun back to its original performances. As a next step we plan to perform emittance measurement with a solenoid scan and EMS near the emission threshold at RT and cryogenic temperature and demonstrate electron beam properties suitable for UED applications.[29] Field emission or voltage breakdown studies at room and cryogenic temperatures aimed at further increasing the energy of the electron beam for non-UED applications might be of interest for accelerator physics community.

In summary, we have demonstrated operation of a HV DC photoemission gun that allows cooling of photocathode down to cryogenic temperatures. This electron source introduces new important features: (i) the gun was specifically designed to minimize the intrinsic emittance (via the photocathode substrate temperature) and to increase the electric field at the photocathode at the same time; (ii) the physical size and the beam

quality of this gun are especially suitable for UED applications as predicted by detailed beam dynamics simulations[29]. Finally, we have successfully generated first beam from the photocathode at both RT and the cryogenic temperature. We believe that this new type of electron source will advance the development of bright electron sources and their applications.

Acknowledgement

The authors thank Tobey Moore and CLASSE machine shop for their technical support. We also acknowledge Colwyn Gulliford, Adam Bartnik, John Dobbins and Peter Quigley for their help and advice. This work has been funded by the National Science Foundation (Grant No. PHY-1416318).

CHAPTER 5

Conclusion

In this thesis, various efforts to develop ultrabright electron sources have been presented in the three key aspects of maximizing electron brightness: lower MTE, smaller initial beam size and larger voltage (and the associated electric field). First, Chapter §2 demonstrated the reduction of MTE via cryogenic cooling of the photocathode substrate. It includes development of the ultra-low emittance diagnostics in order to measure MTEs in the regime where such low MTEs have not been previously well studied. Chapter §3 studies the photoemission property differences of a photocathode for reflection and transmission modes in order to ultize the benefits of transmission cathodes such as micron sized rms laser spots on the cathode. Finally, the construction of a new DC HV photogun was presented in §4. This gun represents a compact HV electron photoemission source equipped with a novel cryogenic scheme. The first beam with energy of ∼200 keV was successfully generated at both RT and 40 K cathode temperatures.

Beyond the efforts and accomplishments presented in this thesis, ultrabright femto-second beams from this source remain to be demonstrated. As a starting point, new emittance measurements will be performed with a solenoid scan and EMS near the emission threshold at RT and cryogenic temperature to demonstrate electron beam properties suitable for UED applications.

The electron source uses will be extended beyond generating ultra bright beams for UED applications. Characterizing the electron beam properties is critical for understanding the

physics of photoemission process and the corresponding material science. The photocathode type that can be used in this gun is not confined to the alkali antimonides grown on a flat surface, but in fact is limitless; e.g. polarized cryogenic photocathodes or field-enhanced photoemissive tips can be tested as well. The photogun presented in chapter §4 will serve as a unique vehicle to understand these specialty electron beams.

The cryogenic photocathode and photogun presented here have contributed to a new type of bright electron sources. Still, this work by no means has exhausted the topic of bright beam production. If anything, it only proved that the possibilities of the photoemission sources and their applications have no boundary and are wide open.

APPENDIX A

Sources of systematic errors of free expansion method

A.1 Sources of systematic errors of free expansion method

In this appendix we describe the issues encountered while implementing this free expansion technique which affect the accuracy of the method.

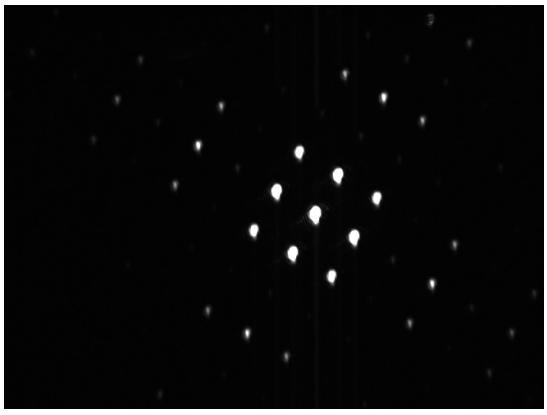

Figure A.1: A diffraction pattern with 473nm laser. This image is taken 5mm away from the grid. A minimum distance between patterns is 250um.

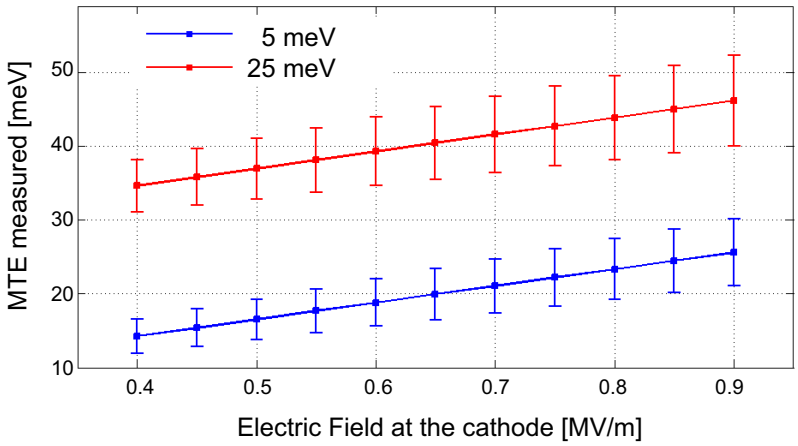

Figure A.2: A diffraction pattern such as Fig. A.1 contributes to incorrect MTE measurements. When the initial MTE is given as shown in the legend, the MTE measured shows the electric field dependence.

A.1.1 Diffraction on the cathode due to the grid

The grid in the anode plays a key role in providing the constant longitudinal electric field while generating no transverse field. However, one issue is that the grid is in the path of the illuminated laser. When the tightly focused laser passes through the grid, it forms a diffraction pattern making the effective spot size larger thus introducing an uncertainty in the MTE measurement.

The diffraction pattern due to the grid (of 12.5 μm spacing) at a distance of 5mm away with 473nm laser is shown in Fig. A.1. We simulated the free expansion technique by using the diffraction pattern as a source instead of the focused spot. The results are shown in Fig. A.2. The effect shows the significant electric field dependence on the low MTEs. The distance between the diffraction spots depends on the wavelength of the laser and grid spacing. Hence it may be possible to avoid this problem by using a bigger grid spacing. The bigger grid spacing may, however, introduce errors related to the focusing from the grid[5].

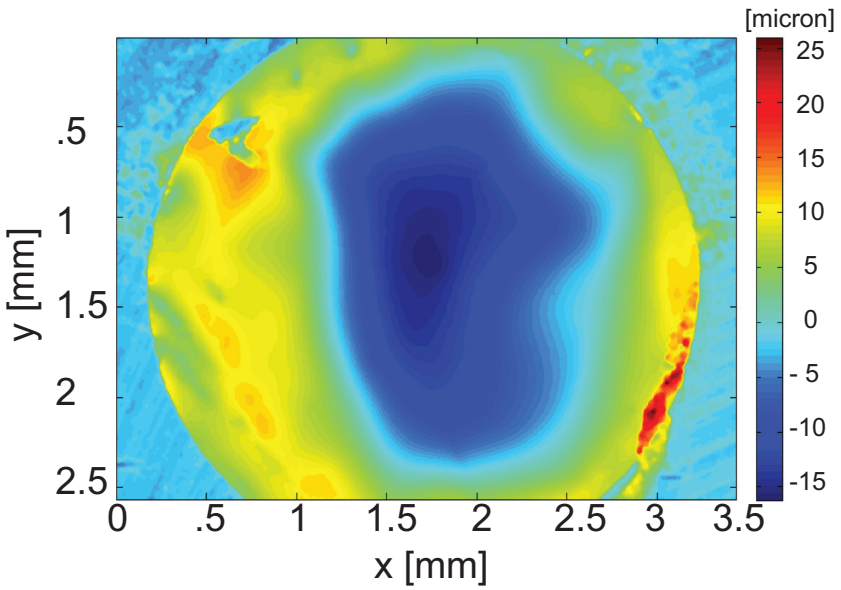

Figure A.3: The grid deformation. This is obtained from a darkfield light microscope.

To avoid this problem we replaced the grid holder with a glass anode coated with 5 nm titanium and allowing the laser to pass through the glass instead of the grid.

A.1.2 Grid non-uniformity

The commercially available grid is thin (10 μm in our case) and gets easily deformed. Fig. A.3 shows the non-uniformity in the flatness of the grid due to the deformation. The free expansion setup in the reference[5] avoided this issue by implementing a stretched electroformed grid, but such a grid is not compatible with the glass anode holder used in the TEmeter. While this non-uniformity exists in the setup, it is difficult to model the exact electric fields in the acceleration region, resulting in the non-uniform grid contributing to an uncertainty in the results.

To ensure an accurate measurement and a small uncertainty we decided to use an anode

with a hole instead of a grid. This enabled us to simulate the setup accurately without having to deal with the uncertainties involved in the grid non-uniformity.

A.2 Stray electric field

They way the anode and the cathode are supported can change the stray field. In our original design, the anode was located on top of the thermal reservoir held by insulators as shown in Fig. A.4 (a). This lead to stray fields in the drift region several cm around the anode. These electric fields were sufficient to cause noticeable emittance growth and lead to erroneous MTE measurements.

To overcome this issue the support for the anode was changed. In the new design the anode was supported by a grounded cylinder that enclosed the drift space beyond the anode and blocked out any stray fields. The new design is shown is Fig. A.4(b).

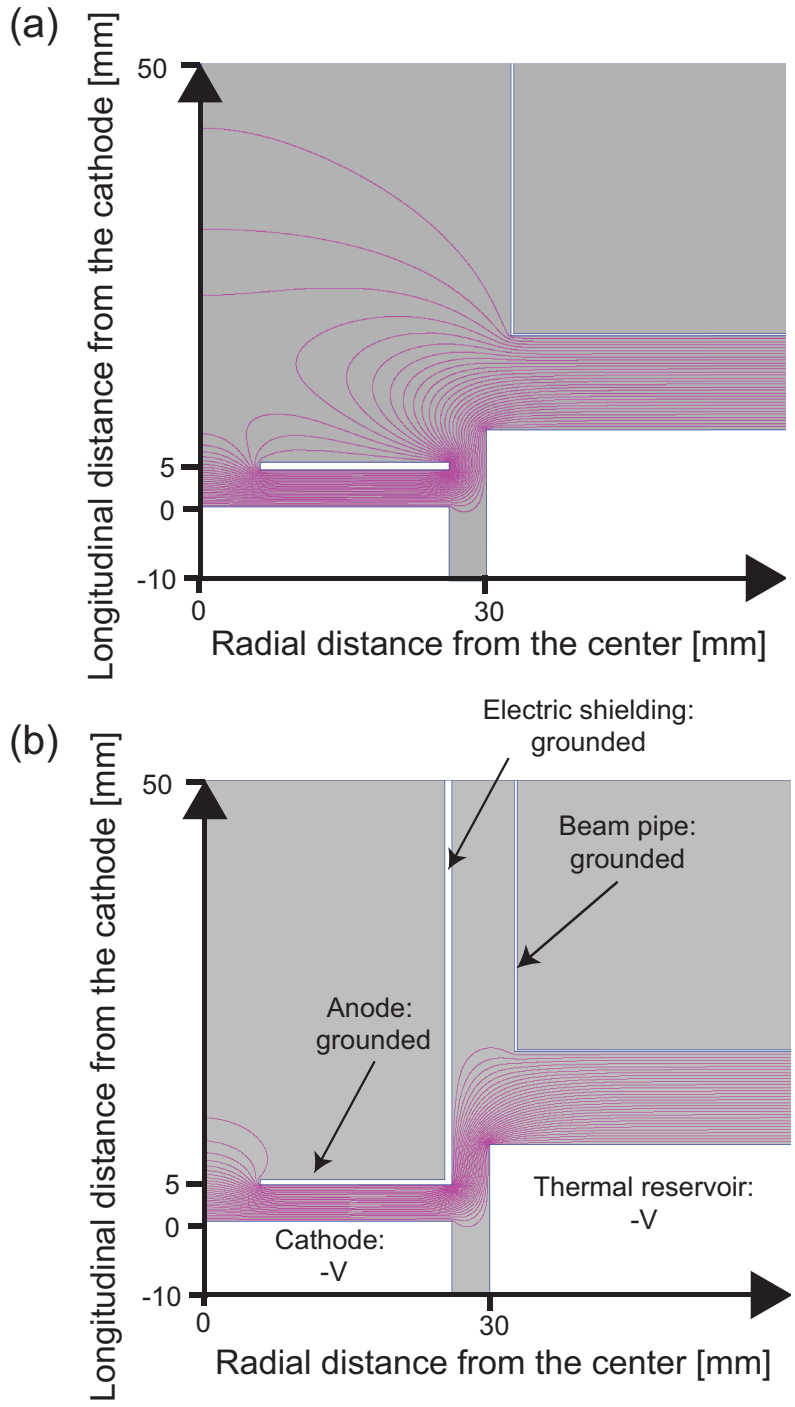

Figure A.4: Comparison between two configuration: (a) shows the electric field line (purple line) without the electric shield and (b) shows the line with the shield (the grounded cylinder).

References

1. D. J. Thompson, D. Murphy, R. W. Speirs, R. M. W. van Bijnen, A. J. McCulloch, R. E. Scholten, and B. M. Sparkes, "Suppression of emittance growth using a shaped cold atom electron and ion source," *Phys. Rev. Lett.* **117** (Nov, 2016) 193202. viii, 6, 7
2. A. D. Palczewski, *Angle-resolved photoemission spectroscopy (ARPES) studies of cuprate superconductors*. PhD thesis, Iowa State University, 2010. viii, 13, 14, 15
3. S. Karkare and et al, "2-d energy analyzer for low energy electrons," *Review of Scientific Instruments* **86** no. 3, (2015) –. viii, 14, 15, 16
4. Ivan V. Bazarov and et al, "Benchmarking of 3d space charge codes using direct phase space measurements from photoemission high voltage dc gun," *Phys. Rev. ST Accel. Beams* **11** (Oct, 2008) 100703. viii, 18
5. J. Feng, J. Nasiatka, W. Wan, T. Vecchione, and H. A. Padmore, "A novel system for measurement of the transverse electron momentum distribution from photocathodes," *Review of Scientific Instruments* **86** no. 1, (2015) –. viii, 14, 20, 34, 70, 71
6. Los Alamos National Laboratory, "Poisson Superfish.". `http://laacg.lanl.gov/laacg/services/download_sf.phtml`. viii, 25, 27
7. T. Vecchione, D. Dowell, "Quantum efficiency and transverse momentum from metals," in *Proceedings of FEL2013, New York, NY, USA*, no. FEL Technology I: Guns, Injectors and Accelerator, pp. 424–426. 2013. ix, 2, 3, 34, 42
8. I. Ben-Zvi and et al, "R&D towards cooling of the RHIC Collider," *Nuclear Instruments and Methods in Physics Research Section A* **532** no. 1–2, (10, 2004) 177–183. 1, 11
9. Sol M. Gruner and et al, "Energy recovery linacs as synchrotron radiation sources (invited)," *Review of Scientific Instruments* **73** no. 3, (2002) 1402–1406. 11
10. W. J. Engelen, M. A. van der Heijden, D. J. Bakker, E. J. D. Vredenbregt, and O. J. Luiten, "High-coherence electron bunches produced by femtosecond photoionization," *Nature Communications* **4** (04, 2013) 1693 EP –. 46
11. D. J. Flannigan and A. H. Zewail, "4d electron microscopy: Principles and applications," *Accounts of Chemical Research* **45** no. 10, (10, 2012) 1828–1839. 1, 2, 46
12. R. D. Miller, "Mapping atomic motions with ultrabright electrons: The chemists' gedanken experiment enters the lab frame," *Annual Review of Physical Chemistry* **65** no. 1, (2014) 583–604. 1, 5, 46, 47
13. M. Gao, C. Lu, H. Jean-Ruel, L. C. Liu, A. Marx, K. Onda, S. Koshihara, Y. Nakano, X. Shao, T. Hiramatsu, G. Saito, H. Yamochi, R. R. Cooney, G. Moriena, G. Sciaini, and R. J. D. Miller, "Mapping molecular motions leading to charge delocalization with ultrabright electrons," *Nature* **496** no. 7445, (04, 2013) 343–346. 2, 46
14. V. R. Morrison, R. P. Chatelain, K. L. Tiwari, A. Hendaoui, A. Bruhács, M. Chaker,

and B. J. Siwick, "A photoinduced metal-like phase of monoclinic vo2 revealed by ultrafast electron diffraction," *Science* **346** no. 6208, (10, 2014) 445.

15. J. Maxson, D. Cesar, G. Calmasini, A. Ody, P. Musumeci, and D. Alesini, "Direct measurement of sub-10 fs relativistic electron beams with ultralow emittance," *Physical Review Letters* **118** no. 15, (04, 2017) 154802–.

16. T. van Oudheusden, *Electron source for sub-relativistic single-shot femtosecond diffraction*. PhD thesis, Department Department of Applied Physics of the Eindhoven University of Technology,, 2010. 8, 63

17. H. Ihee, V. A. Lobastov, U. M. Gomez, B. M. Goodson, R. Srinivasan, C.-Y. Ruan, and A. H. Zewail, "Direct imaging of transient molecular structures with ultrafast diffraction," *Science* **291** no. 5503, (2001) 458–462. 2, 46

18. W. E. Spicer, "Photoemissive, photoconductive, and optical absorption studies of alkali-antimony compounds," *Phys. Rev.* **112** (Oct, 1958) 114–122. 2, 34

19. H. Lee, S. Karkare, L. Cultrera, A. Kim, and I. V. Bazarov, "Review and demonstration of ultra-low-emittance photocathode measurements," *Rev. Sci. Instrum.* **86** no. 7, (2015) . 2, 11, 34, 38, 46, 47

20. L. Cultrera, S. Karkare, H. Lee, X. Liu, I. Bazarov, and B. Dunham, "Cold electron beams from cryocooled, alkali antimonide photocathodes," *Phys. Rev. ST Accel. Beams* **18** (Nov, 2015) 113401. 2, 31, 34, 43, 46, 47

21. I. V. Bazarov, B. M. Dunham, and C. K. Sinclair, "Maximum achievable beam brightness from photoinjectors," *Phys. Rev. Lett.* **102** (Mar, 2009) 104801. 3, 12, 46, 47

22. D. Filippetto, P. Musumeci, M. Zolotorev, and G. Stupakov, "Maximum current density and beam brightness achievable by laser-driven electron sources," *Phys. Rev. ST Accel. Beams* **17** (Feb, 2014) 024201. 3

23. C. Gulliford, A. Bartnik, I. Bazarov, and J. Maxson, "Multiobjective optimization design of an rf gun based electron diffraction beam line," *Phys. Rev. Accel. Beams* **20** (Mar, 2017) 033401. 3

24. Germán Sciaini and R J Dwayne Miller, "Femtosecond electron diffraction: heralding the era of atomically resolved dynamics," *Reports on Progress in Physics* **74** no. 9, (August, 2011) . 4, 5, 46, 47

25. B. Fultz and I. ebrary, *Transmission electron microscopy and diffractometry of materials*. Springer, Berlin, 2008. 5

26. D. H. Dowell, I. Bazarov, B. Dunham, K. Harkay, C. Hernandez-Garcia, R. Legg, H. Padmore, T. Rao, J. Smedley, and W. Wan, "Cathode R & D for future light sources," *Nuclear Instruments and Methods in Physics Research A* **622** (Oct., 2010) 685–697. 6

27. G. Xia, M. Harvey, A. J. Murray, L. Bellan, W. Bertsche, R. B. Appleby, O. Mete, and S. Chattopadhyay, "An ultracold low emittance electron source," *Journal of*

Instrumentation **9** no. 06, (2014) P06011. 6

28. J. M. Maxson, I. V. Bazarov, W. Wan, H. A. Padmore, and C. E. Coleman-Smith, "Fundamental photoemission brightness limit from disorder induced heating," *New Journal of Physics* **15** no. 10, (2013) 103024. 6, 47

29. C. Gulliford, A. Bartnik, and I. Bazarov, "Multiobjective optimizations of a novel cryocooled dc gun based ultrafast electron diffraction beam line," *Phys. Rev. Accel. Beams* **19** (Sep, 2016) 093402. 3, 7, 8, 35, 46, 47, 57, 64, 65, 66

30. I. V. Bazarov, A. Kim, M. N. Lakshmanan, and J. M. Maxson, "Comparison of dc and superconducting rf photoemission guns for high brightness high average current beam production," *Phys. Rev. ST Accel. Beams* **14** (Jul, 2011) 072001. 8, 28

31. J. R. Dwyer, *Femtosecond electron diffraction studies of ultrafast structural dynamics*. PhD thesis, 2005. Copyright - Database copyright ProQuest LLC; ProQuest does not claim copyright in the individual underlying works; Last updated - 2016-03-14. 8

32. T. van Oudheusden, P. L. E. M. Pasmans, S. B. van der Geer, M. J. de Loos, M. J. van der Wiel, and O. J. Luiten, "Compression of subrelativistic space-charge-dominated electron bunches for single-shot femtosecond electron diffraction," *Phys. Rev. Lett.* **105** (Dec, 2010) 264801. 8

33. R. P. Chatelain, V. R. Morrison, C. Godbout, and B. J. Siwick, "Ultrafast electron diffraction with radio-frequency compressed electron pulses," *Applied Physics Letters* **101** no. 8, (2017/05/10, 2012) 081901. 46

34. S. Tokita, M. Hashida, S. Inoue, T. Nishoji, K. Otani, and S. Sakabe, "Single-shot femtosecond electron diffraction with laser-accelerated electrons: Experimental demonstration of electron pulse compression," *Phys. Rev. Lett.* **105** (Nov, 2010) 215004.

35. H. Wiedemann and I. ebrary, *Particle accelerator physics*. Springer, Berlin, Heidelberg, 3 ed., 2007. [electronic resource] / Helmut Wiedemann.; online resource; Includes bibliographical references (p. [925]-935) and index.; License restrictions may limit access. 8

36. W. J. Engelen and et al, "Effective temperature of an ultracold electron source based on near-threshold photoionization," *Ultramicroscopy* **136** no. 0, (2014) 73–80. 11, 12, 14, 18, 37, 38, 46

37. U. J. Lorenz and A. H. Zewail, "Observing liquid flow in nanotubes by 4d electron microscopy," *Science* **344** no. 6191, (06, 2014) 1496–1500. 11

38. J. R. Dwyer and et al, "Femtosecond electron diffraction: making the molecular movie," *Philosophical Transactions of the Royal Society of London A* **364** no. 1840, (March, 2006) 741–778. 11

39. I. V. Bazarov, B. M. Dunham, Y. Li, X. Liu, D. G. Ouzounov, C. K. Sinclair, F. Hannon, and T. Miyajima, "Thermal emittance and response time measurements of negative electron affinity photocathodes," *J. Appl. Phys* **103** (2008) . 12, 14, 18, 24, 37,

65

40. D. H. Dowell and J. F. Schmerge, "Quantum efficiency and thermal emittance of metal photocathodes," *Phys. Rev. ST Accel. Beams* **12** (Jul, 2009) 074201. 34

41. H. J. Qian and et al, "Experimental investigation of thermal emittance components of copper photocathode," *Physical Review Special Topics - Accelerators and Beams* **15** no. 4, (04, 2012) 040102–. 12

42. Siddharth Karkare and et al, "Monte carlo charge transport and photoemission from negative electron affinity gaas photocathodes," *Journal of Applied Physics* **113** no. 10, (2013) –. 12

43. S. Karkare and I. Bazarov, "Effect of nanoscale surface roughness on transverse energy spread from gaas photocathodes," *Applied Physics Letters* **98** no. 9, (2011) –. 12

44. Timothy C. Droubay and et al, "Metal-insulator photocathode heterojunction for directed electron emission," *Phys. Rev. Lett.* **112** (Feb, 2014) 067601. 13, 14

45. Y. Wang, *Laser-based Angle-resolved Photoemission Spectroscopy of Topological Insulators*. PhD thesis, Harvard University, 2012. 13, 14

46. D. Sertore and et al, "Cesium telluride and metals photoelectron thermal emittance measurements using a time-of-flight spectrometer," in *Proceedings of EPAC 2004*. Lucerne, Switzerland, 2004. 13, 14

47. D. A. Orlov, M. Hoppe, U. Weigel, D. Schwalm, A. S. Terekhov, and A. Wolf, "Energy distributions of electrons emitted from gaas(cs,o)," *Applied Physics Letters* **78** no. 18, (2001) 2721–2723. 14, 15

48. V. E. Andreev, A. L. Bukhgeim, A. S. Terekhov, "Recovery of electron velocity distribution in vacuum photodetectors," *Journal of Inverse and Ill-Posed Problems* **7** no. 5, (1999) 427–434. 14, 17

49. V.V. Bakin and et al, "Refraction of thermalized electrons emitted ballistically into vacuum from GaAs-(Cs,O)," *Journal of Experimental and Theoretical Physics Letters* **77** no. 4, (2003) 167–171. 14, 17

50. S. G. Anderson, J. B. Rosenzweig, G. P. LeSage, and J. K. Crane, "Space-charge effects in high brightness electron beam emittance measurements," *Phys. Rev. ST Accel. Beams* **5** (Jan, 2002) 014201. 14, 18, 19

51. C. P. Hauri and et al, "Intrinsic emittance reduction of an electron beam from metal photocathodes," *Physical Review Letters* **104** no. 23, (06, 2010) 234802–. 14, 18

52. M. Reiser, *Theory and design of charged particle beams*. Wiley, New York, 1994. 14, 19, 28

53. C. Gulliford, A. Bartnik, I. Bazarov, L. Cultrera, J. Dobbins, B. Dunham, F. Gonzalez, S. Karkare, H. Lee, H. Li, Y. Li, X. Liu, J. Maxson, C. Nguyen, K. Smolenski, and Z. Zhao, "Demonstration of low emittance in the cornell energy recovery linac injector prototype," *Phys. Rev. ST Accel. Beams* **16** (Jul, 2013) 073401. 14, 19, 60

54. J. Maxson, L. Cultrera, C. Gulliford, and I. Bazarov, "Measurement of the tradeoff between intrinsic emittance and quantum efficiency from a naksb photocathode near threshold," *Appl. Phys. Lett.* **106** no. 23, (2015) . 14, 34, 46, 60

55. L.B. Jones, et al, "The commissioning of tess : An experimental facility for measuring the electron energy distribution from photocathodes," in *Proceedings of FEL2013*, vol. FEL technology 1. New York, NY, USA, 2013. 14, 20, 21

56. M. G. Minty and F. Zimmerman, *Measurement and control of charged particle beams*. Springer, New York, 2003. 18, 37, 65

57. Ivan Bazarov and et al, "Thermal emittance measurements of a cesium potassium antimonide photocathode," *Applied Physics Letters* **98** no. 22, (2011) –. 18, 24

58. R. K. Li and et al, "Nanometer emittance ultralow charge beams from rf photoinjectors," *Phys. Rev. ST Accel. Beams* **15** (Sep, 2012) 090702. 19

59. H. Li, *Multi-dimensional characterization of the laser and electron beams of the Cornell Energy Recovery Linac photoinjector prototype*. PhD thesis, Cornell University, 2012. 19

60. L. Cultrera, et al, "Photocathode R&D at Cornell University," in *Proceedings of IPAC2012*. New Orleans, Louisiana, USA, 2012. 23

61. Pulsar Physics, "General particle tracer (gpt).". `http://www.pulsar.nl/gpt/`. 25

62. H. Lee, L. Cultrera, and I. Bazarov, "Intrinsic emittance reduction in transmission mode photocathodes," *Applied Physics Letters* **108** no. 12, (2017/05/17, 2016) 124105. 33

63. S. Schubert, M. Ruiz-Osés, I. Ben-Zvi, T. Kamps, X. Liang, E. Muller, K. Müller, H. Padmore, T. Rao, X. Tong, and et al, "Bi-alkali antimonide photocathodes for high brightness accelerators," *APL Mater.* **1** no. 3, (2013) . 34, 46

64. E. Wang, T. Rao, and I. Ben-zvi, "Enhancement of photoemission from and postprocessing of k2cssb photocathode using excimer laser," *Phys. Rev. ST Accel. Beams* **17** (Feb, 2014) 023402. 34, 46

65. B. Dunham, J. Barley, A. Bartnik, I. Bazarov, L. Cultrera, J. Dobbins, G. Hoffstaetter, B. Johnson, R. Kaplan, S. Karkare, and et al, "Record high-average current from a high-brightness photoinjector," *Appl. Phys. Lett.* **102** no. 3, (2013) . 34

66. C. Gulliford, A. Bartnik, I. Bazarov, B. Dunham, and L. Cultrera, "Demonstration of cathode emittance dominated high bunch charge beams in a dc gun-based photoinjector," *Appl. Phys. Lett.* **106** no. 9, (2015) . 34

67. N. Yamamoto, X. G. Jin, A. Mano, T. Ujihara, Y. Takeda, S. Okumi, T. Nakanishi, T. Yasue, T. Koshikawa, T. Ohshima, and et al, "Status of the high brightness polarized electron source using transmission photocathode," *Journal of Physics: Conference Series* **298** no. 1, (2011) 012017. 36

68. M. Kuwahara, S. Kusunoki, X. G. Jin, T. Nakanishi, Y. Takeda, K. Saitoh, T. Ujihara, H. Asano, and N. Tanaka, "30-kv spin-polarized transmission electron microscope with

gaas–gaasp strained superlattice photocathode," *Appl. Phys. Lett.* **101** no. 3, (2012) . 36

69. L. Cultrera, H. Lee, and I. Bazarov, "Alkali antimonides photocathodes growth using pure metals evaporation from effusion cells," *J. Vac. Sci. Technol. B* **34** no. 1, (2016) . 36, 60

70. J. Maxson, I. Bazarov, B. Dunham, J. Dobbins, X. Liu, and K. Smolenski, "Design, conditioning, and performance of a high voltage, high brightness dc photoelectron gun with variable gap," *Rev. Sci. Instrum.* **85** no. 9, (2014) . 37, 55, 63

71. A. Ebina and T. Takahashi, "Transmittance spectra and optical constants of alkali-antimony compounds k3sb, na3sb, and na2ksb," *Phys. Rev. B* **7** (May, 1973) 4712–4719. 40

72. K. L. Jensen, B. L. Jensen, E. J. Montgomery, D. W. Feldman, P. G. O'Shea, and N. Moody, "Theory of photoemission from cesium antimonide using an alpha-semiconductor model," *J. Appl. Phys* **104** no. 4, (2008) . 41

73. M. B. Tzolov and M. N. Iliev, "Raman scattering from monoalkali (na-sb and k-sb), bialkali (na-k-sb) and multialkali (na-k-sb-cs) photocathodes," *Thin Solid Films* **213** no. 1, (1992) 99 – 102. 41

74. R. Feynman, R. Leighton, and M. Sands, *The Feynman Lectures on Physics*, vol. 1. Addison-Wesley, Boston, second ed., 1963. 43

75. Hyeri Lee, Xianghong Liu, Luca Cultrera, Ivan Bazarov, Bruce Dunham, Vaclav O. Kostroun, "A cryogenically cooled high voltage dc photoemission accelerator," *Physical Review Accelerators and Beams* (2017) . 45

76. A. J. McCulloch, D. V. Sheludko, M. Junker, and R. E. Scholten, "High-coherence picosecond electron bunches from cold atoms," *Nature Communications* **4** (04, 2013) 1692 EP –. 46

77. B. J. Siwick, J. R. Dwyer, R. E. Jordan, and R. J. D. Miller, "Ultrafast electron optics: Propagation dynamics of femtosecond electron packets," *Journal of Applied Physics* **92** no. 3, (2017/05/11, 2002) 1643–1648. 47

78. D. Murphy, R. E. Scholten, and B. M. Sparkes, "Increasing the brightness of cold ion beams by suppressing disorder-induced heating with rydberg blockade," *Phys. Rev. Lett.* **115** (Nov, 2015) 214802. 47

79. F. O. Kirchner, S. Lahme, F. Krausz, and P. Baum, "Coherence of femtosecond single electrons exceeds biomolecular dimensions," *New Journal of Physics* **15** no. 6, (2013) 063021. 47

80. W. E. King, G. H. Campbell, A. Frank, B. Reed, J. F. Schmerge, B. J. Siwick, B. C. Stuart, and P. M. Weber, "Ultrafast electron microscopy in materials science, biology, and chemistry," *Journal of Applied Physics* **97** no. 11, (2005) 111101, `http://dx.doi.org/10.1063/1.1927699`. 47

81. V. Pishchik, *Sapphire : Material, Manufacturing, Applications*. Springer US, Boston, MA, 2009. 51

82. G. R. Werner, *Probing and Modeling Voltage Breakdown in Vacuum*. PhD thesis, Cornell University, 2014. 52, 55

83. S. M. Gerbick, M. P. Kelly, "A clean pumping and venting system for srf cavities and cryomodules," in *Proceedings of SRF2009, Berlin, Germany*, no. 08 Ancillary systems, pp. 619–621. 2009. 53

84. K. Zapfe, J. Wojtkiewicz, "Particle free pump down and venting of uhv vacuum systems," in *Proceedings of SRF2007, Peking Univ., Beijing, China*, no. WEP: Poster Session II, pp. 681–684. 2007. 53

85. R. Arora and W. Mosch, *High voltage and electrical insulation engineering*. J. Wiley and Sons, Hoboken, N.J., 2011. 55

86. N. Nishimori, I. Bazarov, B. Dunham, J. Grames, C. Hernandez-Garcia L. Jones, B. Militsyn, M. Poelker, K. Surles-Law, M. Yamamoto, "Erl09 wg1 summary: Dc gun technological challenges," in *Proceedings of ERL09, Ithaca, NY, USA*, no. Injectors, Guns, and Cathodes, pp. 4–23. 2009. 55

87. I. V. Bazarov, B. M. Dunham, C. Gulliford, Y. Li, X. Liu, C. K. Sinclair, K. Soong, and F. Hannon, "Benchmarking of 3d space charge codes using direct phase space measurements from photoemission high voltage dc gun," *Phys. Rev. ST Accel. Beams* **11** (Oct, 2008) 100703. 65

88. S. Belomestnykh, I. Bazarov, V. Shemelin, J. Sikora, K. Smolenski, and V. Veshcherevich, "Deflecting cavity for beam diagnostics at cornell erl injector," *Nuclear Instruments and Methods in Physics Research Section A: Accelerators, Spectrometers, Detectors and Associated Equipment* **614** no. 2, (3, 2010) 179–183. 65